ACID: A Comprehensive Toolbox for Image Processing and Modeling of Brain, Spinal Cord, and Post-mortem Diffusion MRI Data

Gergely David[1,2*], Björn Fricke[1*], Jan Malte Oeschger[1], Lars Ruthotto[3], Patrick Freund[2,4,5], Karsten Tabelow[6], Siawoosh Mohammadi[1,4†]

[1] Department of Systems Neurosciences, University Medical Center Hamburg-Eppendorf, Hamburg, Germany

[2] Spinal Cord Injury Center, Balgrist University Hospital, University of Zurich, Zurich, Switzerland

[3] Department of Mathematics, Emory University, Atlanta, GA, USA

[4] Wellcome Trust Centre for Neuroimaging, University College London, London, United Kingdom

[5] Department of Neurophysics, Max Planck Institute for Human Cognitive and Brain Sciences, Leipzig, Germany

[6] Weierstrass Institute for Applied Analysis and Stochastics, Berlin, Germany

*Shared first authors.

[†]Corresponding author at Department of Systems Neurosciences, University Medical Center Hamburg-Eppendorf, Martinistrasse 52, 20246 Hamburg, Germany, +49 (0) 40 7410 59859, s.mohammadi@uke.de

Björn Fricke, Department of Systems Neurosciences, University Medical Center Hamburg-Eppendorf, Martinistrasse 52, 20246 Hamburg, Germany, Phone: +49 (0) 40 7410 59859, bj.fricke@uke.de

Abstract

Diffusion MRI (dMRI) has become a crucial imaging technique within the field of neuroscience and has an increasing number of clinical applications. Although most studies still focus on the brain, there is a growing interest in utilizing dMRI to investigate the healthy or injured spinal cord. The past decade has also seen the development of biophysical models that link MR-based diffusion measures to underlying microscopic tissue characteristics. Building upon 13 years of research and development, we present an open-source, MATLAB-based academic software toolkit dubbed ACID: A Comprehensive Toolbox for Image Processing and Modeling of Brain, Spinal Cord, and Post-mortem Diffusion MRI Data. ACID is designed to process and model dMRI data of the brain, spinal cord, and post-mortem specimens by incorporating state-of-the-art artifact correction tools, diffusion and kurtosis tensor imaging, and biophysical models that enable the estimation of microstructural properties in white matter. Additionally, the software includes an array of linear and non-linear fitting algorithms for accurate diffusion parameter estimation. By adhering to the Brain Imaging Data Structure (BIDS) data organization principles, ACID facilitates standardized analysis, ensures compatibility with other BIDS-compliant software, and aligns with the growing availability of large databases utilizing the BIDS format. Furthermore, ACID seamlessly integrates into the popular Statistical Parametric Mapping (SPM) framework, benefitting from a wide range of established segmentation, spatial processing, and statistical analysis tools as well as a large and growing number of SPM extensions. As such, this comprehensive toolbox covers the entire processing chain from raw DICOM data to group-level statistics, all within a single software package.

1. Introduction

Diffusion MRI (dMRI) exploits the self-diffusion of water molecules to produce images that are sensitive to tissue microstructure by measuring the diffusion along various spatial directions (Callaghan et al., 1988; Le Bihan et al., 1988; Stejskal & Tanner, 1965). dMRI has been applied to study a number of phenomena including normal brain development (Dubois et al., 2014; Miller et al., 2002), aging (Draganski et al., 2011; Sullivan et al., 2010), training-induced plasticity (Scholz et al., 2009), and monitoring progression of and recovery from neurological diseases (Farbota et al., 2012; Meinzer et al., 2010). Clinical applications of dMRI include the diagnosis of ischemic stroke (Urbach et al., 2000), multiple sclerosis (Horsfield et al., 1996), cancer and metastases (Gerstner and Sorensen, 2011), and surgical planning of brain tumors (Chun et al., 2005). Although the vast majority of dMRI applications has focused on the brain, there is a growing interest in spinal cord dMRI, as researchers seek sensitive and predictive markers of spinal cord white matter damage (Cohen et al., 2017; Martin et al., 2016).

To fully utilize the sensitivity of dMRI to tissue microstructure, expert knowledge is required to minimize artifacts both during acquisition, e.g., by cardiac gating or twice-refocused spin-echo sequences, and through dedicated post-processing methods. Commonly used post-processing techniques include motion and eddy current correction (Andersson & Sotiropoulos, 2016; Mohammadi et al., 2010), susceptibility distortion correction (Gu & Eklund, 2019; Ruthotto et al., 2012), denoising (Becker et al., 2014; Veraart et al., 2016), Rician bias correction (Oeschger et al., 2023a; Sijbers et al., 1998), and robust tensor fitting techniques (Chang et al., 2005; Mohammadi et al., 2013). Retrospective artifact correction techniques, along with diffusion signal modeling capabilities, are widely available in open-source toolboxes such as FSL-FDT (Smith et al., 2004), DiPY (Garyfallidis et al., 2014), DESIGNER (Ades-Aron et al., 2018), ExploreDTI (Leemans et al., 2009), MRtrix3 (Tournier et al., 2019), TORTOISE (Pierpaoli et al., 2010), AFNI-FATCAT (Taylor & Saad, 2013), and others.

However, currently available toolboxes have one or more shortcomings. The majority of toolboxes have been developed for brain dMRI and may not work for spinal cord dMRI, which features higher level and different nature of artifacts (Barker, 2001; Stroman et al., 2014), or post-mortem dMRI of tissue specimens, which have different and highly varying geometry (see Sébille et al., 2019 for a list of post-mortem dMRI studies). Although there are some software options available for processing spinal cord images, most notably the Spinal Cord Toolbox (De Leener et al., 2017), these tools lack comprehensive artifact correction and biophysical modeling capabilities for estimation of microstructural diffusion properties related to microscopic tissue properties. Biophysical modeling directly estimates these microstructural properties (e.g., axonal water fraction and orientation dispersion) as aggregated measures on voxel-level and thereby offers greater specificity than standard diffusion tensor (DTI) or diffusion kurtosis imaging (DKI). Toolboxes dedicated for biophysical modelling

of the dMRI signal, such as the NODDI (Zhang et al., 2012) or SMI toolbox (Coelho et al., 2022), typically do not include a comprehensive processing pipeline to correct for artifacts in dMRI data. In addition, only a few of the aforementioned dMRI toolboxes support the Brain Imaging Data Structure (BIDS, Gorgolewski et al., 2016) standard for organizing and annotating raw and processed dMRI data. The lack of standardization complicates not only the sharing and aggregation of processed dMRI data but also the application of automated image analysis tools designed for big data, such as machine learning techniques. Over the past two decades, tens of thousands of dMRI datasets have been made openly available in large neuroimaging databases (e.g., HCP (Van Essen et al., 2013) and the UK Biobank (Littlejohns et al., 2020)), underscoring the importance of consistent data storage practices.

Building upon 13 years of research and development, we introduce the open-source MATLAB-based ACID toolbox: A Comprehensive Toolbox for Image Processing and Modeling of Brain, Spinal Cord, and Post-mortem Diffusion MRI Data. ACID was initially developed as a collection of artifact correction tools but has now been extended to a comprehensive toolbox for processing and modeling of dMRI data. In particular, ACID offers (i) state-of-the-art image processing tools as well as (ii) DTI, DKI, and biophysical model parameter estimation methods optimized for brain, spinal cord, and post-mortem dMRI data. Additionally, (iii) ACID adheres to the BIDS standard for organizing the output, making the processed images compliant with other BIDS software and facilitating data sharing. Finally, (iv) ACID is embedded in the Statistical Parametric Mapping (SPM) framework, benefitting from its established functions including spatial processing tools and statistical inference schemes. ACID tools can be combined with other SPM tools to create pipelines in SPM's batch processing system, which offers an all-in-one software solution from conversion of DICOM data to statistical group analysis. Many of the methods used in the ACID toolbox have already been published in the scientific dMRI literature (Table 1). In this paper, we detail the design and function of the ACID modules, along with guidance on their optimal combination for brain, spinal cord, and post-mortem applications.

Table 1. Peer-reviewed methods of the ACID toolbox.

Method	Introduced in
ECMOCO: Eddy current and motion correction	Mohammadi et al., 2010
HySCO: Susceptibility artifact correction	Ruthotto et al., 2012
msPOAS: Adaptive denoising	Becker et al., 2014
RBC: Rician bias correction	Oeschger et al., 2023a
DTI using robust fitting	Mohammadi et al., 2013
DKI and axisymmetric DKI using NLLS	Oeschger et al., 2023a, 2023b
NODDI-DTI	Edwards et al., 2017
WMTI-Watson	Oeschger et al., 2023b
Reliability masking	David et al., 2017

Abbreviations: DTI, diffusion tensor imaging; DKI, diffusion kurtosis imaging; NLLS, non-linear least squares; NODDI, neurite orientation dispersion and density imaging; WMTI, white matter tract integrity.

2. Methods

2.1 Installation and toolbox documentation

The ACID toolbox is an extension of SPM12 that requires existing MATLAB and SPM12 installations. The toolbox has been developed and tested with MATLAB versions R2017b to R2023a and SPM12 from versions r6906 onwards. It is recommended to use the latest SPM release, which can be downloaded from the SPM website[1], as developments in ACID are synchronized with those in SPM.

Information about the toolbox can be found on the main project website[2]. The source code is available on Bitbucket[3], where the latest version as well as all previous versions of the toolbox can be downloaded. There are three ways to install the toolbox: (i) by cloning the repository (recommended for staying up-to-date with the latest release), (ii) by downloading the toolbox as a zip file and placing the unzipped directory into the `spm12/toolbox` directory, or (iii) by downloading the toolbox as a zip file and using a redirection script that enables switching between different local versions of ACID. The full documentation of the toolbox is available as a Wiki on the git repository[4], which provides detailed installation instructions, module descriptions, and step-by-step instructions for a typical analysis pipeline.

ACID is free but copyrighted software, distributed under the terms of the GNU General Public License as published by the Free Software Foundation (either version 2 of the License or, at your option, any later version). Further details on "copyleft" can be found at the GNU website[5]. It should be noted that ACID is supplied as is and no formal support or maintenance is provided. The toolbox was

[1] http://www.fil.ion.ucl.ac.uk/spm/software/spm12/
[2] http://www.diffusiontools.com/
[3] https://bitbucket.org/siawoosh/acid-artefact-correction-in-diffusion-mri
[4] https://bitbucket.org/siawoosh/acid-artefact-correction-in-diffusion-mri/wiki/Home
[5] http://www.gnu.org/copyleft/

developed for academic research purposes only and comes with no warranty, nor is it intended for clinical and diagnostics use.

2.2 Organization of the toolbox

The ACID modules can be found in the SPM12 Batch Editor by navigating to `SPM -> Tools -> ACID Toolbox`. The toolbox is divided into six modules, as shown in Fig. 1: *Startup*, *Pre-processing*, *Diffusion tensor/kurtosis imaging*, *Biophysical models*, *Utilities, and External tools*. A brief description of each module is provided below.

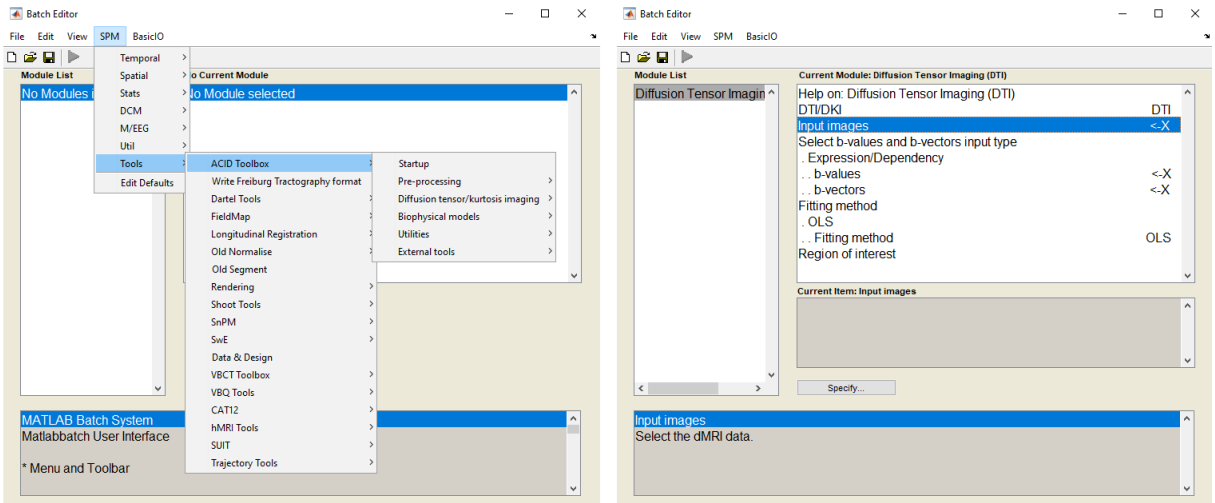

Fig. 1. The left panel shows the location of ACID toolbox in the SPM Batch Editor after successful installation (`SPM -> Tools`). The toolbox is organized into six modules, each of which may be further divided into submodules. The right panel provides an example of a submodule (*Diffusion Tensor Imaging* within the *Diffusion tensor/kurtosis imaging* module). Each (sub-) module requires at least one mandatory input, indicated by "X", as well as several optional inputs and parameter settings, which can be adjusted for customization.

2.3 Startup

The ACID modules rely on a set of default settings, which were selected to yield reasonable results for typical dMRI data. However, adjustments may be necessary depending on the specific dataset (see Section 3.2 for recommendations). For convenience, the module's graphical user interface (GUI) only presents the settings that are likely to be modified. Advanced users can access and modify all settings through the script `config/local/acid_local_defaults.m`. To use modified settings, the *Startup* module must be executed with the customized file provided as input; these settings will remain in effect even after restarting SPM or MATLAB until new settings are specified.

ACID requires all input images to be in uncompressed NIfTI format (either NIfTI-1 or NIfTI-2), and all dMRI images to be in 4D NIfTI format. Users can convert from DICOM to NIfTI format using SPM's DICOM Import function, which can also export metadata into JSON files if the "Export metadata" option is enabled. To bring dMRI data into the required format, the *Startup* module can be utilized to (i) convert a set of 3D NIfTI files into a single 4D NIfTI file, (ii) generate corresponding bval/bvec files

from the JSON files (if not already available), (iii) create an additional metadata file containing the most commonly reported subject and acquisition parameters (such as TE and TR) to provide a concise overview of the dataset, and (iv) set an output directory alternative to the default one. The output from *Startup* (4D NIfTI file and corresponding bval/bvec files) can be automatically passed to subsequent processing steps through dependencies.

2.4 Pre-processing

In the following sections, we provide a brief description of each artifact correction tool implemented in ACID. For specific recommendations regarding different dMRI datasets (brain, spinal cord, post-mortem/ex vivo), refer to Sections 3.2 and 4.1.

2.4.1 Eddy current and motion correction (ECMOCO)

ACID uses the eddy current and motion correction (ECMOCO) algorithm (Mohammadi et al., 2010) to correct for spatial misalignments that may occur between the dMRI volumes. These misalignments can be caused by motion and eddy currents induced by the rapidly varying field of the diffusion-sensitizing gradients (Jezzard et al., 1998), which may lead to biased diffusion estimates (Mohammadi et al., 2013). ECMOCO aligns all source volumes to a target volume using a co-registration algorithm (Friston & Ashburner, 1997) implemented in the SPM function *spm_coreg*. It was previously shown that the robustness of registration can be increased by separately registering diffusion-weighted (DW) and non-diffusion-weighted (b0) volumes to their corresponding target volumes (Mohammadi et al., 2015a). ECMOCO features the multi-target registration mode, where source volumes from each diffusion shell (b-value) are co-registered to their shell-specific target volume (Fig. A1). ECMOCO rotates the b-vectors by the obtained rotational parameters; the rotated b-vectors can be passed on to subsequent processing steps.

In spinal cord dMRI, eddy current and motion correction is more challenging than in brain dMRI due to the considerably lower number of voxels and lower signal-to-noise ratio (SNR), particularly in volumes with high b-values (>1000 s/mm^2) or with diffusion-sensitizing gradients parallel to the spinal cord. While movement of the brain can be considered rigid to the first approximation, the spinal cord may experience varying degrees of displacement along the rostro-caudal axis caused by factors such as breathing, pulsation of the cerebrospinal fluid, or swallowing (Yiannakas et al., 2012). To address this, we introduced *slice-wise* (2D) registration, which independently aligns each slice of the source volume to the corresponding slice of the target volume, thereby correcting for non-rigid, slice-dependent displacements. For more details on ECMOCO, including other recently introduced features (*initialized registration* and *exclusion mode*), refer to Appendix A.

2.4.2 Adaptive denoising (msPOAS)

Multi-shell Position-Orientation Adaptive Smoothing (msPOAS) is an iterative adaptive denoising algorithm designed to adaptively reduce noise in dMRI data while preserving tissue boundaries without introducing blurring (Becker et al., 2012, 2014; Tabelow et al., 2015). The algorithm adapts to the intensity values and their distance in both voxel space and the spherical space of diffusion directions, allowing smoothing only within spatially homogeneous areas of the DW images. One of the key advantages of msPOAS is its compatibility with all diffusion models as it operates on the raw dMRI data. Adjustable parameters include *kstar* (number of iterations that define the image smoothness), *lambda* (adaptation parameter that defines the strength of edge detection), *kappa* (initial ratio of the amount of smoothing between the local space of neighboring voxels and the spherical space of diffusion gradients), and *ncoils* (parallel imaging factor, i.e., the number of receiver coils that contributed to the measured signal). To distinguish random fluctuations from structural differences, msPOAS requires an estimate of SNR, or equivalently the noise standard deviation (*sigma*). A higher *kstar* leads to greater smoothness within homogeneous image regions, while a larger *lambda* results in weaker adaptation and more blurring at tissue edges. The optimal *kappa* depends on the number of directions per shell, while *ncoils* should be the same as the value used for noise estimation. When using msPOAS, we recommend starting with the default parameters and the *sigma* estimated with the *Noise estimation* utility function (Table 2). In case of insufficient noise reduction, parameters should be adjusted according to Appendix C.

2.4.3 Rician bias correction

The voxel intensities of MRI magnitude images exhibit a Rician distribution in case of a single receiver coil (Gudbjartsson & Patz, 1995) and a non-central χ distribution in case of multiple receiver coils (Aja-Fernández et al., 2014). When fitting diffusion signal models (Section 2.5), this distribution leads to a bias, known as the Rician bias, in the estimated tensor (Basser & Pajevic, 2000; Gudbjartsson & Patz, 1995; Jones & Basser, 2004) and kurtosis parameters (Veraart et al., 2011; Veraart et al., 2013a), such as an overestimation of kurtosis. This Rician bias is particularly relevant in low SNR situations (Polzehl & Tabelow, 2016). Two approaches of Rician bias correction (RBC) are implemented in ACID. The M2 approach, introduced in (Miller & Joseph, 1993) and later extended to multi-channel receiver coil (André et al., 2014), operates on the dMRI data and uses the second moment of the non-central χ distribution of the measured intensities and noise estimates to estimate the true voxel intensities. The second approach modifies the parameter estimation by considering the non-central χ distribution to account for the Rician bias during model fitting (Oeschger et al., 2023a). Note that the latter approach assumes uncorrected data, therefore it must not be combined with the first method and is currently only available for non-linear least squares fitting. Both methods require an estimate of the noise standard deviation, which can be obtained using the *Noise estimation* utility function, either by the

standard or the *repeated measures* method (Table 2). While we generally recommend using the *repeated measures* method, it requires the acquisition of several b0 images and is therefore not applicable if only a single b0 image is available. In addition, ACID offers the *Rician bias simulation* utility function to determine the optimal RBC method for the dMRI dataset and SNR at hand (Table 2).

2.4.4 Susceptibility artifact correction (HySCO)

Hyperelastic Susceptibility Artifact Correction (HySCO) is a technique used to correct for geometric distortions caused by susceptibility artifacts (Ruthotto et al., 2012, 2013). These artifacts can occur at interfaces between tissues with different magnetic susceptibilities, such as those found near paranasal sinuses, temporal bone, and vertebral bodies. To correct for these artifacts, HySCO estimates the bias field based on a reversed-gradient spin-echo echo planar imaging (EPI) acquisition scheme. This requires the acquisition of at least one image with identical acquisition parameters as the dMRI data but with opposite phase-encoding direction. The obtained bias field map is then applied to the entire dMRI data to unwarp the geometric distortions. For datasets that include a full blip-reversed acquisition, the submodule *HySCO: combine blip-up and blip-down images* is recommended for a more accurate correction of susceptibility artefacts.

2.5 Diffusion signal models

The dependence of dMRI signal on the direction and strength of diffusion-weighting is commonly described by mathematical models. Two of the most widely used models are DTI (Basser et al., 1994) and DKI (Hansen et al., 2016; Jensen et al., 2005).

2.5.1 Diffusion tensor imaging (DTI)

DTI describes the anisotropic water diffusion in the white matter by a diffusion tensor with six independent diffusion parameters. The eigenvalues of the tensor can be used to compute rotationally invariant DTI scalar metrics including fractional anisotropy (FA) and mean (MD), axial (AD), and radial diffusivities (RD). The interpretation of DTI assumes that the direction of axial diffusivity is aligned with the white matter tracts, which may not be the case in complex fiber geometry such as crossing or fanning fibers.

ACID provides four algorithms to obtain the diffusion tensor (see Appendix D for details). Ordinary least squares (OLS) fits the tensor model by minimizing the sum of squared model-fit errors, while weighted least squares (WLS) minimizes the *weighted* sum of squared model-fit errors, accounting for the distortion of noise distribution in the logarithmized data. Robust fitting is similar to WLS but factorizes the weights into three components to account for local and slice-specific artifacts as well, while also featuring Tikhonov regularization to handle ill-conditioned weighting matrices resulting from a high occurrence of outliers. Robust fitting is designed to downweigh outliers in the model fit, which can otherwise introduce a bias in the fitted model parameters (Mohammadi et al.,

2013) (Fig. D1). Unlike the linearized models, the non-linear least squared (NLLS) method is based on an implementation (Modersitzki, 2009) of the Gauss-Newton algorithm and operates on the non-logarithmic data, avoiding the distortion of noise distribution.

2.5.2 Diffusion kurtosis imaging (DKI)

DKI expands the diffusion tensor model by the kurtosis tensor, a fourth-order tensor with 15 independent parameters, which captures the effects of non-Gaussian water diffusion. From the 15 kurtosis parameters, several kurtosis metrics can be estimated including the mean of the kurtosis tensor (MW), the axial (AW), and radial kurtosis (RW) (Tabesh et al., 2011), as well as the apparent mean (MK), axial (AK), and radial kurtosis (RK) (Fig. 2). These metrics provide additional information about tissue complexity beyond what can be captured by tensor metrics alone. DKI requires the acquisition of a second diffusion shell with higher b-value (typically between 1000 and 2500 s/mm^2). ACID also includes the axisymmetric DKI model, a recent modification of DKI which reduces the parameter space to 8 independent parameters by imposing the assumption of axisymmetrically distributed axons (Hansen et al., 2016).

Note that the diffusion tensor parameters from DKI might differ from standard DTI parameters. In particular, diffusivities (AD, MD, and RD) derived from the DTI model are often underestimated compared to those derived from the DKI model (referred to as kurtosis bias) (Edwards et al., 2017). By incorporating higher-order moments of the diffusion signal, DKI can address kurtosis bias, resulting in more accurate diffusivities (see Appendix F for a comparison of MD derived from DTI and DKI).

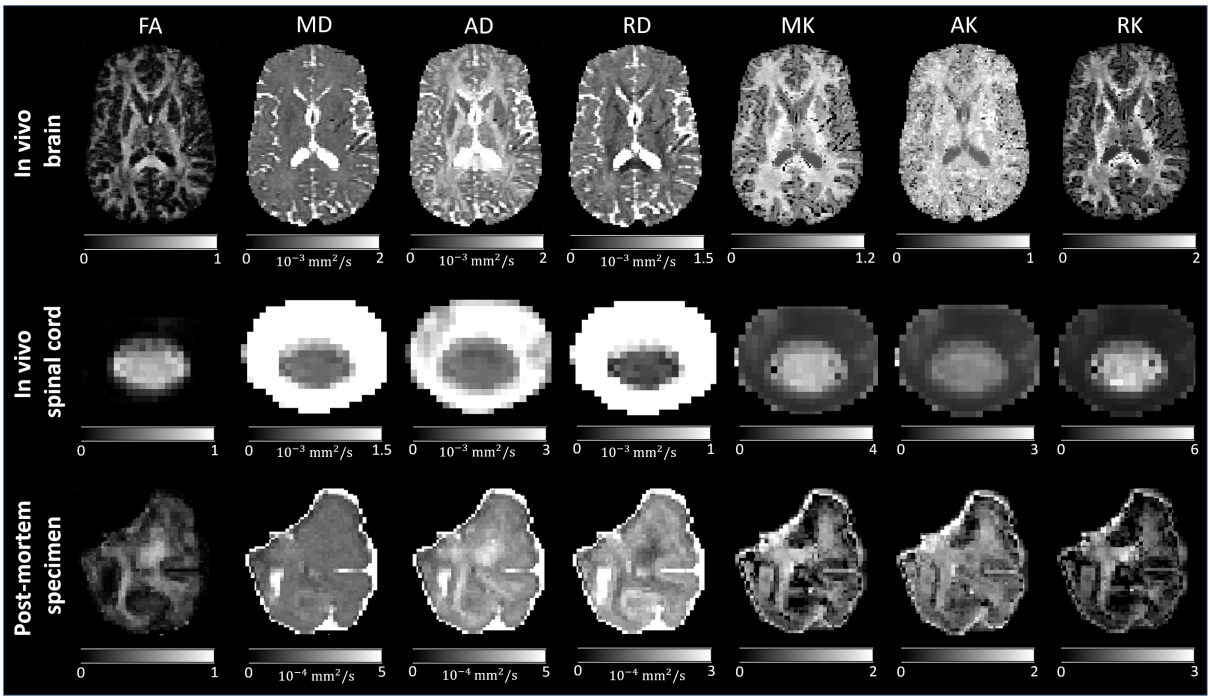

Fig. 2. Selected maps derived from diffusion kurtosis imaging (DKI) using an in vivo brain, in vivo spinal cord, and post-mortem dMRI dataset (refer to Section 3.2 for details on the dataset). Shown are maps of fractional

anisotropy (FA), mean diffusivity (MD), axial diffusivity (AD), radial diffusivity (RD), apparent mean kurtosis (MK), apparent axial kurtosis (AK), and apparent radial kurtosis (RK).

2.6 Biophysical models

Biophysical models separate the dMRI signal into distinct signal components from various tissue compartments, each with their own underlying assumptions. Biophysical models provide more specific and biologically interpretable metrics that are directly linked to tissue microstructure (Jelescu et al., 2020). The application of biophysical models is often referred to as dMRI-based in vivo histology (Mohammadi & Callaghan, 2021; Weiskopf et al., 2021) or microstructural dMRI (Jelescu et al., 2020; Novikov, 2021; Novikov et al., 2019). In the following, we briefly describe the two biophysical models currently implemented in ACID (WMTI-Watson and NODDI-DTI), while recommendations on their usage are provided in Section 4.2.2. Example maps are shown in Fig. 3, and specific values obtained from the brain and spinal cord are presented in Appendix H.

2.6.1 WMTI-Watson model

The white matter tract integrity (WMTI)-Watson model as an implementation of the Standard Model assumes two non-exchanging water compartments (intra- and extra-axonal tissue water) (Alexander et al., 2019; Novikov et al., 2019). The model characterizes the intra-axonal compartment as "sticks" of zero radius, with an intra-axonal diffusivity D_a and axonal water fraction f. Axon alignment (or orientation dispersion) is modeled using the Watson distribution parameter κ. The extra-axonal space is modeled as a homogenous medium, described by an axisymmetrical diffusion tensor with parallel ($D_{e,\parallel}$) and perpendicular ($D_{e,\perp}$) extra-axonal diffusivities. The five biophysical parameters (D_a, f, κ, $D_{e,\parallel}$, $D_{e,\perp}$) are derived from the axisymmetric DKI tensor metrics ($D_\parallel$, $D_\perp$, $W_\parallel$, $W_\perp$, W) according to the formulas described in (Jespersen et al., 2018; Novikov et al., 2018). Being derived from the biophysical Standard Model, the estimation of WMTI-Watson biophysical parameters is generally degenerate, which leads to two solutions: the plus branch, which assumes $D_a > D_{e,\parallel}$, and the minus branch, which assumes $D_a < D_{e,\parallel}$. We recommend using the plus branch (default in the toolbox), as in our experience, and also reported by others (Jelescu et al., 2020; Jespersen et al., 2018), the minus branch is the biologically invalid solution.

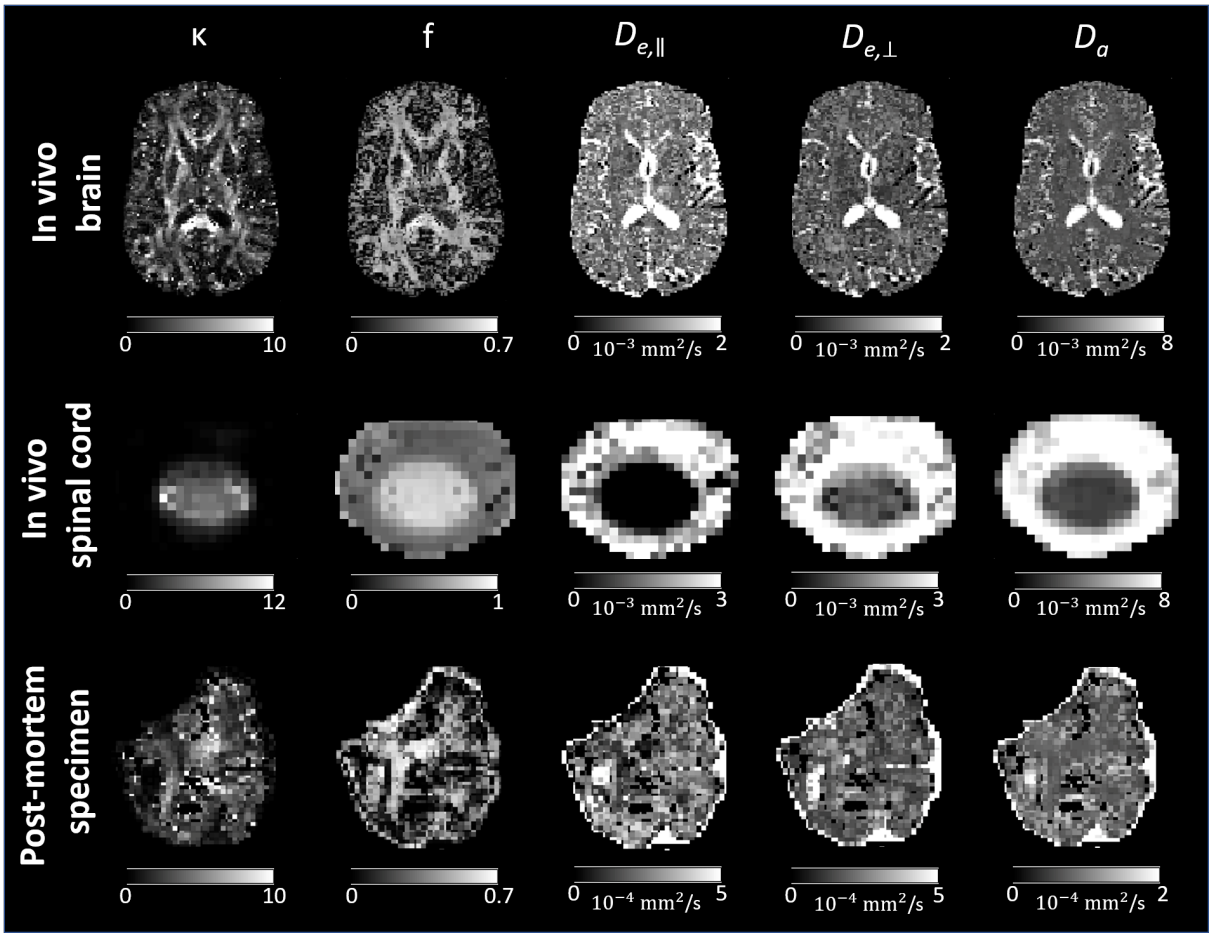

Fig. 3. Maps of biophysical parameters derived from the WMTI-Watson model using an in vivo brain, in vivo spinal cord and post-mortem dMRI dataset (refer to Section 3.2 for details on the dataset). Shown are maps of axon orientation dispersion (κ), axonal water fraction (f), parallel and perpendicular extra-axonal diffusivities ($D_{e,\parallel}$ and $D_{e,\perp}$), and intra-axonal diffusivity (D_a). Note that for the in vivo spinal cord dataset, the maximum b-value (b=1500 s/mm^2) was too low for accurate estimation of $D_{e,\parallel}$, resulting in voxels with negative values within the spinal cord.

2.6.2 NODDI-DTI

NODDI-DTI (Edwards et al., 2017) is based on the neurite orientation dispersion and density imaging (NODDI) model (Zhang et al., 2012). While NODDI is a three-compartment biophysical model with intra- and extra-axonal space, and cerebrospinal fluid compartments, NODDI-DTI assumes that the latter compartment can be neglected in normal appearing white matter. It further assumes fixed compartmental diffusivities: $D_{e,\parallel}$=D_a=1.7 μm^2/ms and $D_{e,\perp}$=(1-f)·$D_{e,\parallel}$. NODDI-DTI estimates the intra- (f or v_{ic}) and extra-neurite ($1-f$) signal fraction as well as the Watson distribution parameter κ from single-shell data, whereas both NODDI and WMTI-Watson require specific multi-shell dMRI data for robust parameter estimation.

2.7 Utilities

ACID offers a variety of utility functions for image manipulation, mask generation, quality assessment, and other related tasks (refer to Table 2 for more details).

Table 2. List of the ACID utility functions.

FUNCTION	DESCRIPTION
Image cropping	Crops images to a smaller size for less storage space and faster processing. *Inputs*: images to crop, new matrix size, and voxel coordinates of the center of cropping. The center of cropping can also be selected manually through a pop-up window. *Outputs*: cropped images and the cropping parameters. Cropping is particularly useful for spinal cord dMRI, where the spinal cord occupies a small part of the image. When using reduced field-of-view sequences, cropping is typically only necessary in the frequency-encoding direction.
Resample to dimension	Resamples images to the desired resolution. *Inputs*: images to be resampled, desired resolution, and type of interpolation. *Output*: resampled images.
Slice-wise realignment	Allows for manual translation and scaling of images along the x and y directions, on a slice-by-slice basis, facilitated by intensity contour lines of the source image overlaid on the target image. *Inputs*: a single image to be realigned, target image, and other images to which the realignment parameters are applied. *Outputs*: realigned image(s) and the realignment parameters. It is particularly helpful for realigning spinal cord images, where residual misalignment is often slice-dependent.
Make brain mask	Creates a binary brain mask by (i) segmenting the brain image into gray matter, white matter, and cerebrospinal fluid using SPM12's unified segmentation (Ashburner & Friston, 2005), (ii) summing up the resulting probability maps, and (iii) thresholding it at a certain value (default: 0.8). *Input*: brain image. *Output*: binary brain mask.
Reliability masking	Aims to identify "unreliable" voxels, i.e., voxels irreversibly corrupted by artifacts. Reliability masks are generated by thresholding the map of root-mean-square model-fit error (rms(ε)) (David et al., 2017). *Inputs*: maps of rms(ε) (output by tensor fitting with label: RMS-ERROR) and the desired threshold value. *Outputs*: a binary "reliability mask" that can be used in region-of-interest (ROI)-based analyses. The optimal threshold can be determined using the *Determine* threshold submodule. Reliability masking is a supplementary outlier rejection technique that can be applied after each model fitting method. It is particularly useful in scenarios where many data points are affected by outliers (often the case in spinal cord dMRI), which could otherwise lead to unstable tensor fits and inaccurate tensor estimates.
DWI series browser	Allows to browse through the slices of the dMRI data for quality assessment. Slices with low SNR and/or artifacts can be identified and labeled. The saved labels can be used to inform ECMOCO about unreliable slices (see *Exclusion mode* in Appendix A).
DWI series movie	Allows to simultaneously stream the images of dMRI datasets in a video mode for quality assessment. It can be used either to visually assess a single dMRI dataset or to compare the images before vs. after a certain processing step (e.g., ECMOCO). *Inputs*: up to three dMRI datasets. *Output*: a video file containing the image streams.
Noise estimation	Estimates the noise standard deviation (σ) in the dMRI data using either the *standard* or the *repeated measures method*. The *standard method* uses the formula $\sigma \approx \sqrt{\sum_{i \,\epsilon\, mask} S_i^2 \,/(2Ln)}$, where S_i is the voxel intensity within a background mask defined outside the body, L is the number of voxels within the background mask,

	and n is the parallel imaging factor, i.e., the effective number of coil elements that contributed to the measured signal (Constantinides et al., 1997). The *repeated measures method* uses the formula: $\sigma \approx \mathrm{mean}_r\left(\mathrm{std}_\mathrm{k}\left(S(i,k)\right)\right)$, where $S(i,k)$ is the voxel intensity at voxel i in the kth repeated image (Dietrich et al., 2007). The standard deviation and mean operators are performed across the repetitions and voxels, respectively. The set of repeated images can be either the non-diffusion-weighted (b≈0) or strongly diffusion-weighted (the highest b-value) images (see Appendix B for recommendations). *Inputs*: the raw (unprocessed) dMRI dataset, a mask (*standard method*: background mask; *repeated measures method*: see Appendix B), *n* (for the *standard method* only), and b-values (for the *repeated measures method* only). *Output*: a single σ, assuming a homogeneous variance. Recommendations for noise mask generation can be found on the wiki page.
Rician bias simulation	Simulates diffusion-weighted MRI signals at specified SNR values in voxels within the brain white and gray matter. The simulated signals are corrected using specified Rician bias correction (RBC) methods (for details, see Oeschger et al., 2023a). *Inputs*: a voxel (from a list of 27 pre-defined voxels, each with different diffusivities), a list of SNR values, and the number of repetitions. *Output*: a figure displaying the distance between the estimated metric and the ground truth value for each RBC method.
ROI analysis	Calculates the mean values within a specified region of interest (ROI). *Inputs*: list of images for ROI analysis, and various types of ROIs including (i) global ROIs, applied on all images in the list, (ii) subject-specific ROIs, applied only on the corresponding image, and (iii) reliability masks (see entry *Reliability masking*). The user has the option to specify one or multiple types of ROIs. In the latter case, the function will apply the intersection of selected ROIs. The function offers flexibility for a range of ROI-based analyses; for example, ROI-based analysis in the native space requires a set of subject-specific ROIs, while a single global mask is sufficient in the template space (with optional reliability masks in both cases). *Output*: an array containing the mean values per subject, ROI, and (optionally) slice.
Fusion	Merges two images with different field of views (FOV), such as a brain and a spinal cord image, into a single combined image. *Inputs*: two images to be merged and a target image (typically a structural image with a larger FOV). *Output*: a combined image, resampled according to the target image. The intensity in overlapping regions is the average of the two intensities. Note that before merging the images, they must be in the correct spatial position; if needed, image realignment can be performed using the SPM *Realign* or the *Slice-wise realignment* utility function.

2.8 External tools

ACID provides the option to integrate external tools from other packages, which can be accessed directly from the ACID GUI (*External tools* module), ensuring a seamless integration into ACID pipelines. We included the following external tools in the current release, which we considered as particularly valuable additions: FSL eddy[6] (Andersson & Sotiropoulos, 2016), Koay noise estimation[7], and the WMTI model (part of the DESIGNER toolbox) (Fieremans et al., 2011).

[6] https://fsl.fmrib.ox.ac.uk/fsl/fslwiki/eddy
[7] https://github.com/jan-martin-mri/koays-inversion

2.9 Output structure and naming convention

ACID supports the BIDS standard, while also being compatible with non-BIDS data. Following BIDS recommendations, ACID appends a label to the output filename's `desc` field, indicating the applied processing step (refer to Table 3 for a list of labels used in the modules *Pre-processing*, *Diffusion tensor/kurtosis imaging*, and *Biophysical models*). For instance, after applying ECMOCO to `sub01_dwi.nii`, the output file becomes `sub01_desc-ECMOCO_dwi.nii`. When multiple processing steps are involved, the labels are concatenated, as in `sub01_desc-ECMOCO-msPOAS_dwi.nii`. Model fitting appends three labels indicating the type of diffusion model, algorithm, and parametric map, such as `sub01_desc-ECMOCO-POAS-DKI-OLS-FA_dwi.nii`. For BIDS-compliant input, ACID generates a bval and bvec file after each processing step. ACID stores all output in the `derivatives` folder, with separate subfolders for each module's output (e.g., `derivatives/POAS-Run`). Even if non-BIDS input is provided, ACID retains the same folder structure and naming convention.

Table 3. List of labels in the output filename's `desc` field within ACID.

Label	Description	Label	Description
ECMOCO	*Eddy Current and Motion Correction*	V1	*1st Eigenvector of the Diffusion Tensor*
msPOAS	*Multi-shell Position-Orientation Adaptive Smoothing*	V2	*2nd Eigenvector of the Diffusion Tensor*
RBC	*Rician Bias Correction*	V3	*3rd Eigenvector of the Diffusion Tensor*
HySCO	*Hyperelastic Susceptibility Artifact Correction*	DKI	*Diffusion Kurtosis Imaging*
fmap	*Off-Resonance Field*	DKIax	*Axisymmetric Diffusion Kurtosis Imaging*
COMB-WM	*Write Combined Weighted Mean*	MK	*Mean Kurtosis*
COMB-AM	*Write Combined Arithmetic Mean*	AK	*Apparent Axial Kurtosis*
DTI	*Diffusion Tensor Imaging*	RK	*Apparent Radial Kurtosis*
OLS	*Ordinary Least Squares*	MW	*Mean of the Kurtosis Tensor*
WLS	*Weighted Least Squares*	AW	*Axial Kurtosis*
ROB	*Robust Tensor Fitting*	RW	*Radial Kurtosis*
NLLS	*Non-linear Least Squares*	WMTI-W	*WMTI-Watson*
FA	*Fractional Anisotropy*	NODDI-DTI	*Neurite Orientation Density and Dispersion - Diffusion Tensor Imaging*
MD	*Mean Diffusivity*		
AD	*Axial Diffusivity*	AWF	*Axon Water Fraction*
RD	*Radial Diffusivity*	DA	*Intra-axonal Diffusivity*
L1	*1st Eigenvalue of the Diffusion Tensor*	DE-PARA	*Parallel Extra-axonal Diffusivities*
L2	*2nd Eigenvalue of the Diffusion Tensor*	DE-PERP	*Perpendicular Extra-axonal Diffusivities*
L3	*3rd Eigenvalue of the Diffusion Tensor*	KAPPA	*Axon/Neurite Orientation Dispersion*

2.10 Quality assessment

We highly recommended assessing the data quality before and after each processing step. In addition to the quality assessment utility functions *DWI series browser* and *DWI series movie* (Table 2), multiple ACID modules generate diagnostic plots to identify the presence and type of artifacts in the dMRI data. Example diagnostic plots are provided in Appendix E.

3. Results

3.1 Pipelines

ACID is fully integrated into the SPM12 batch system, allowing users to execute its functions individually or combined into linear pipelines with multiple steps. Each step can receive the output of any of the previous steps via flexible and easy-to-use dependencies. While pipelines are typically set up in the SPM Batch Editor, they can also be converted into MATLAB code (SPM batch script) for automation and further customization. In addition to its own functions, ACID integrates seamlessly with a range of standard SPM features, including segmentation, co-registration, normalization, and voxel-based statistical analyses, as well as a growing number of SPM extensions[8]. For instance, ACID can be combined with the hMRI toolbox (Tabelow et al., 2019) for multi-modal analysis of dMRI and quantitative MRI data acquired within the same imaging session, all in a single pipeline.

3.2 Example applications

To demonstrate the application of ACID toolbox on different types of dMRI data, here we provide three example pipelines for in vivo brain, in vivo spinal cord, and post-mortem dMRI (Fig. 4). Details of these three datasets are summarized in Table 4. Note that "blip-up" data were available for all three datasets, which refers to the acquisition of either a single b0 volume or all volumes with identical geometry and sequence parameters but opposite phase encoding direction. All example pipelines consist of artifact correction (ECMOCO, msPOAS, RBC, HySCO) and model fitting steps. While the pipelines for brain, spinal cord, and post-mortem dMRI follow similar concepts, recommended settings for each region may differ (Table 5). It is important to note that the settings listed in Table 5 serve as initial values for typical datasets. The optimal settings for a particular dataset depend on the sequence parameters, the subject, and the imaged region. Model fitting may be followed by spatial processing, such as co-registration to the structural image or normalization to a template, and statistical analysis (e.g., ROI- or voxel-based analysis).

[8] https://www.fil.ion.ucl.ac.uk/spm/ext/

Table 4. Scan parameters of the in vivo brain, in vivo spinal cord, and post-mortem dMRI datasets used in this paper.

Dataset	**In vivo brain**	**In vivo spinal cord**	**Post-mortem specimen**
Imaged body part or tissue	entire brain (incl. cerebellum) of a 34-year-old healthy volunteer	upper cervical cord (appr. C1-C4) of a 43-year-old healthy volunteer	post-mortem specimen of the temporal lobe from an epilepsy patient, embedded in phosphate buffered saline
Scanner	3T Siemens Prisma Fit	3T Siemens Prisma Fit	3T Siemens Prisma Fit
Receive coils	64-channel Head/Neck	64-channel Head/Neck	16-channel Hand/Wrist
Sequence	2D single-shot spin-echo EPI	2D single-shot spin-echo EPI	2D single-shot spin-echo EPI
Volumes and b-values [s/mm^2]	30x b=600; 45x b=1100; 60x b=2500; 18x b=0 [*n*=153]	30x b=500; 30x b=1000; 30x b=1500; 11x b=0 [*n*=101]	30x b=600; 75x b=1100; 45x b=2200; 60x 2500; 60x b=5000; 36x b=0 [*n*=306]
Cardiac gating	-	2 slices per cycle, trigger delay of 260 ms	-
Slices	100 (interleaved, no gap)	14 (interleaved, no gap)	
Resolution [mm^3]	1.7 x 1.7 x 1.7	1.0 x 1.0 x 5.0	0.8 x 0.8 x 0.8
Field of view [mm^3]	204 x 170 x 201	128 x 36 x 70	128 x 48 x 48
Echo time	75 ms	73 ms	99 ms
Repetition time	5800 ms	pulse-dependent (cardiac gated)	8700 ms
Parallel imaging	2x (GRAPPA)	-	-
Multi-band	-	-	-
Phase partial Fourier	7/8	-	7/8
Phase-encoding dir.	A-P	A-P	A-P
Readout bandwidth	1842 Hz/pixel	1396 Hz/pixel	802 Hz/pixel
EPI spacing	0.77 ms	0.93 ms	1.37 ms
EPI factor	120	36	60
Acquisition time [min:sec]	17:46	06:51 (nominal)	93:10
Existence of a "blip-up" dataset	One b0 volume with opposite phase-encoding direction	All volumes with opposite phase-encoding direction	All volumes with opposite phase-encoding direction

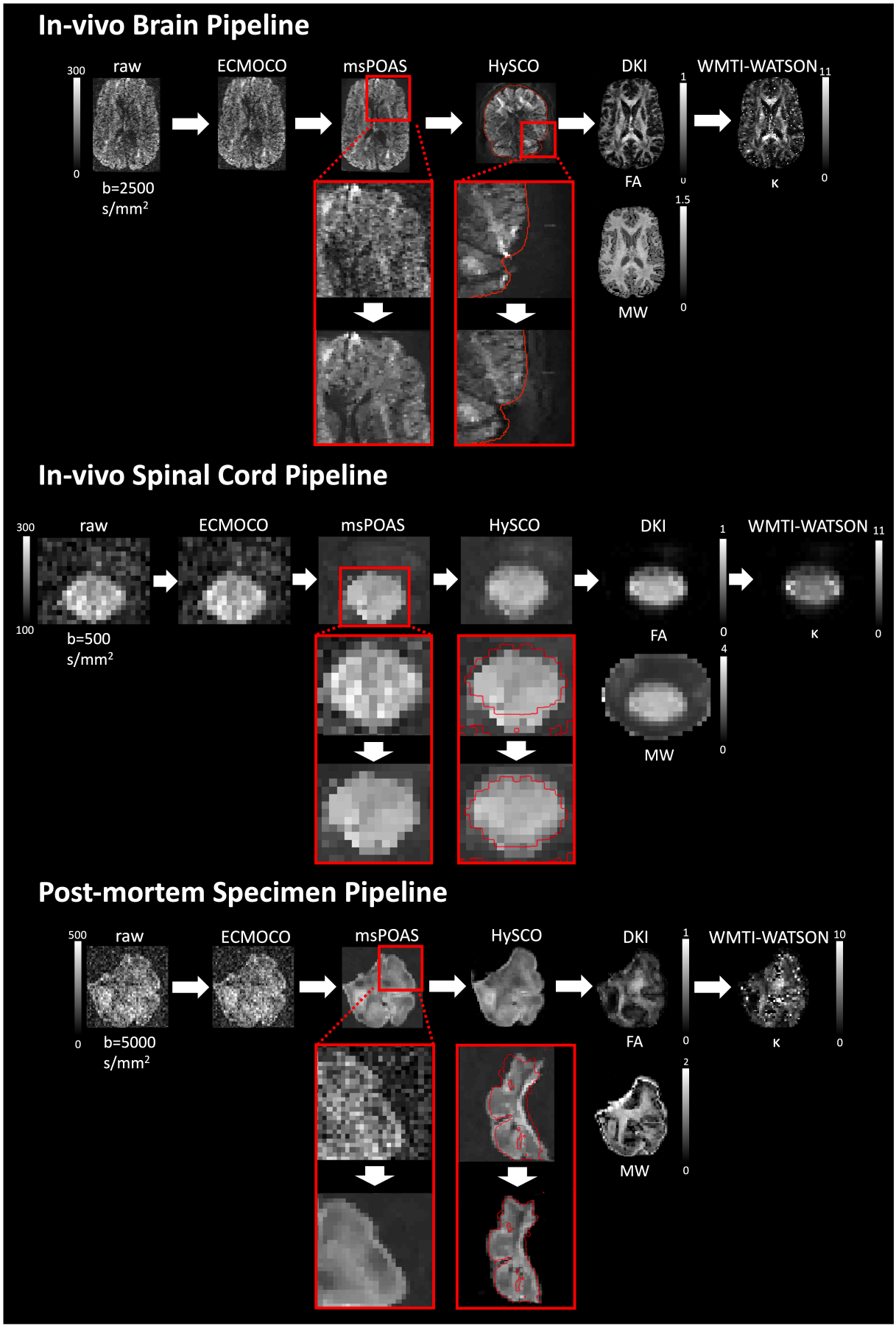
In-vivo Brain Pipeline
raw
ECMOCO
msPOAS
HySCO
DKI
WMTI-WATSON
300
0
b=2500
s/mm²
1
0
FA
11
0
K
1.5
0
MW
In-vivo Spinal Cord Pipeline
raw
ECMOCO
msPOAS
HySCO
DKI
WMTI-WATSON
300
100
b=500
s/mm²
1
0
FA
11
0
K
4
0
MW
Post-mortem Specimen Pipeline
raw
ECMOCO
msPOAS
HySCO
DKI
WMTI-WATSON
500
0
b=5000
s/mm²
1
0
FA
10
0
K
2
0
MW

Fig. 4. Standard processing pipelines for typical in vivo brain, in vivo spinal cord, and post-mortem dMRI datasets (refer to Table 4 for details on the datasets). Although not explicitly shown here, noise estimation should be performed on the raw (unprocessed) data, which serves as input for msPOAS, Rician bias correction, and diffusion tensor fitting (for fitting methods WLS and robust fitting). However, in case of substantial misalignments across volumes, and when using the *repeated measures* noise estimation method, it might be beneficial to perform this step after ECMOCO to prevent an overestimation of noise. For msPOAS, a zoomed-in visual comparison is shown between a diffusion-weighted (DW) image before (middle row) and after applying msPOAS (bottom row); the msPOAS-corrected image appears less noisy while preserving tissue edges. For HySCO, contour lines of the corresponding structural image (displayed as red lines) are overlaid on a zoomed-in DW image both before (middle row) and after applying HySCO (bottom row). HySCO improves the alignment between the DW and the structural image. Note that HySCO is applied as the final pre-processing step; however, the HySCO field map used for "unwrapping" the images is estimated on the ECMOCO-corrected datasets. Rician bias correction (not explicitly shown here) should be applied either before (recommended: between msPOAS and HySCO) or during model fitting. Diffusion signal models are fitted on the processed dataset; here, we display the maps of fractional anisotropy (FA) and mean of the kurtosis tensor (MW) from diffusion kurtosis imaging (DKI). The output from DKI can be used to compute biophysical parameters of the white matter; shown here is the map of axon orientation dispersion (κ) from the WMTI-Watson biophysical model.

Table 5. Settings of selected modules for in vivo brain, in vivo spinal cord, and post-mortem dMRI datasets.

Module	Adjustable parameter	In vivo brain dMRI	In vivo spinal cord dMRI	Post-mortem dMRI
ECMOCO	*type of registration*	volume-wise	volume- and slice-wise	volume-wise
	degrees of freedom	9 [transl. x, y, z ; rotation x, y, z ; scaling y; shearing x-y, y-z]	*volume-wise*: 4 [transl. x, y, z; scaling y] *slice-wise*: 3 per slice [transl. x, y; scaling y]	4 [transl. y; scaling y; shearing x-y, y-z]
msPOAS	*kappa*	automatically determined	increase default for low SNR data (e.g., +20%)	automatically determined
RBC		defaults	defaults	defaults
HySCO		defaults	defaults	defaults
DTI	*Fitting algorithm*	robust fitting or NLLS	robust fitting or NLLS	NLLS
DKI/axDKI	*Fitting algorithm*	NLLS	NLLS	NLLS
NODDI-DTI	*Fixed diffusivities*	In vivo parameters	In vivo parameters	Ex vivo parameters
WMTI-Watson		defaults	defaults	defaults

Notes: In the "degrees of freedom" settings (ECMOCO), x, y, and z represent the frequency-, phase-, and slice-encoding directions, respectively.

4. Discussion

We have developed the ACID toolbox, which extends the capabilities of the SPM framework by providing comprehensive artifact correction and model fitting techniques for brain, spinal cord, and post-mortem dMRI data. Besides commonly used diffusion signal models such as DTI and DKI, ACID also offers biophysical models that provide parameters of white matter tissue microstructure such as axonal water fraction and axon orientation dispersion. Being seamlessly integrated into the SPM batch system, ACID allows for user-friendly access to SPM's powerful spatial processing tools and statistical framework. In addition to offering recommended pipelines for brain, spinal cord, and post-mortem dMRI, ACID provides the flexibility for users to create custom pipelines tailored to their specific data. Adhering to the BIDS conventions facilitates data sharing, enhances data comprehension for investigators, and makes ACID compliant with software requiring BIDS-compliant input (https://bids-apps.neuroimaging.io).

4.1 Considerations for artifact corrections

ACID offers artifact correction steps typically applied on dMRI, including image realignment (ECMOCO), denoising (msPOAS), correction for susceptibility-induced geometric distortions (HySCO), and Rician bias correction (RBC). Here, we discuss specific considerations regarding their use for various applications.

Correcting for displacements within the dMRI data through image realignment is one of the most important but also challenging steps. ECMOCO provides users with the flexibility to choose the degrees of freedom for image realignment based on the anticipated type of displacement, but also offers a selection of pre-defined degrees of freedom that are optimized for brain, spinal cord, and post-mortem dMRI.

In brain dMRI, motion can be approximated as a rigid body displacement with 6 degrees of freedom (DOF). Eddy-current spatial displacements, to a first-order approximation, result in translation and scaling along y and in-plane and through-plane shearing (assuming y to be the phase-encoding direction) (Mohammadi et al., 2010). Since these displacements affect the entire brain similarly, we recommend employing a 9-DOF volume-wise (volume to volume) registration with translation and rotation along x, y, and z, scaling along y, and shearing in the x-y and y-z planes. First-order approximation of eddy-current displacements might not always be sufficient, as dMRI data can also be affected by higher-order eddy-current displacements causing non-linear distortions (Andersson & Sotiropoulos, 2016; Rohde et al., 2004). For example, in our observations, ECMOCO was not effective in removing pronounced eddy-current displacements present in the dMRI data of the Human Connectome Project (Van Essen et al., 2012). In such cases, we recommend using FSL eddy, which incorporates higher-order correction terms (Andersson & Sotiropoulos, 2016) and can be called directly from ACID as an external tool (Section 2.8).

In spinal cord dMRI, volume-wise registration has been found to be less effective (Cohen-Adad et al., 2009; Mohammadi et al., 2013) due to displacements that vary along the rostro-caudal axis of the spinal cord. These displacements appear mostly in the phase-encoding direction and are caused by physiological factors such as respiration and cardiac pulsation (Kharbanda et al., 2006; Summers et al., 2006). We recommend applying volume-wise registration for rough alignment and correction of through-slice displacements, followed by slice-wise (slice to slice) registration for correcting any remaining slice-dependent displacement. This combined approach has demonstrated effectiveness in realigning not only volumes but also individual slices (Fig. A2), as well as improving the contrast-to-noise ratio between gray and white matter and reducing test-retest variability in DTI maps of the spinal cord (Mohammadi et al., 2013). Eddy-current distortions are typically less severe in the spinal cord compared to the brain, because the in-plane field of view is smaller and located near the scanner isocenter. This makes the first-order approximation of eddy-current displacements, as supported by ECMOCO, generally adequate. We recommend employing a 4-DOF volume-wise registration (translation along x, y, z; scaling along y) followed by a 3-DOF slice-wise registration (translation along x, y; scaling along y). In datasets with low SNR, slice-wise correction along x can be omitted, given the smaller range of movement which makes reliable estimation difficult. We discourage correcting for in-plane rotation and shearing, as their expected range is very small. The correction for these DOFs might introduce spurious displacements during realignment, which we consider to be a greater risk than not applying correction at all. Structures surrounding the spinal cord (bones, ligaments, etc.) may move independently from the spinal cord, potentially leading to inaccuracies in transformation parameters. Moreover, as these structures typically occupy a larger portion of the image, they can dominate the estimation of transformation parameters. To address this challenge, ECMOCO provides the option of specifying a spinal cord mask to restrict the estimation of transformation parameters to the spinal cord only. Any residual misalignments can be manually corrected using the *Slice-wise realignment* utility function (Table 2).

In post-mortem dMRI, specimen motion is not anticipated if the specimen is appropriately fixed, for instance, by using a sample holder or embedding it in agarose. Thus, we recommend correcting only for the four first-order eddy-current displacements (y-translation, y-scaling, x-y shearing, y-z shearing). The first-order approximation is typically adequate for small specimens where eddy-current displacements are not severe.

In general, the performance of msPOAS and HySCO is largely independent of the anatomical features present in the image; therefore, default parameters are expected to work well for both brain, spinal cord, and post-mortem dMRI data. It has been noted that HySCO stands out in its ability to reduce susceptibility distortions in spinal cord dMRI when compared to other susceptibility distortion correction tools such as TOPUP (Snoussi et al., 2021). Nevertheless, the default regularization

parameters (alpha "diffusion" and beta "Jacobian" regulator), accessible via the script `config/local/acid_local_defaults.m`, are optimized for the brain and may require adjustment for the spinal cord if performance is inadequate.

Applying HySCO is particularly important for acquisitions with severe susceptibility-related distortions, such as multi-band EPI without parallel imaging, and for multi-contrast analyses where dMRI data or other quantitative maps are combined with structural reference images, e.g., the dMRI-based axonal water fraction and magnetization transfer saturation maps in g-ratio mapping (Mohammadi & Callaghan, 2021) or multi-contrast MRI in the spinal cord (David et al., 2019). In these cases, HySCO improves the overlap between the undistorted structural image and the dMRI data, leading to better performance of subsequent co-registration and normalization algorithms. HySCO also improves the accuracy of g-ratio mapping; for example, the g-ratio can be significantly biased if susceptibility distortions are not adequately corrected (Clark et al., 2021; Mohammadi et al., 2015b).

4.2 Considerations for model fitting

4.2.1 Physical diffusion models

At a given b-value, the SNR in spinal cord dMRI is typically lower than in brain dMRI due to (i) the smaller cross-sectional area that requires higher in-plane resolution (see Fig. 5A for a size comparison), (ii) the high signal attenuation for diffusion-gradient directions parallel to the highly aligned fibers in the head-feet direction (Fig. 5B), (iii) the high prevalence of signal outliers caused by cardiac, respiratory, and other physiological artifacts, and (iv) the suboptimal coil configuration in the thoracic and lumbar regions, which are not covered by the head and neck coil. Lower SNR increases the variance of parameter estimates and makes spinal cord dMRI more susceptible to Rician bias. Consequently, SNR is often prohibitively low at higher b-values necessary for fitting the kurtosis tensor, making the application of DKI in the spinal cord very challenging.

The application of adaptive denoising (msPOAS) is important as it reduces the variance and therefore improves the precision of the tensor and kurtosis parameter estimates (see Appendix G for examples). Rician bias correction, whether applied on the raw data or during model fitting, mitigates the Rician bias in parameter estimates, resulting in more realistic parameter estimates (see Appendix G for examples). A more in-depth analysis of the impact of Rician bias correction on DKI and axisymmetric DKI can be found in (Oeschger et al., 2023a).

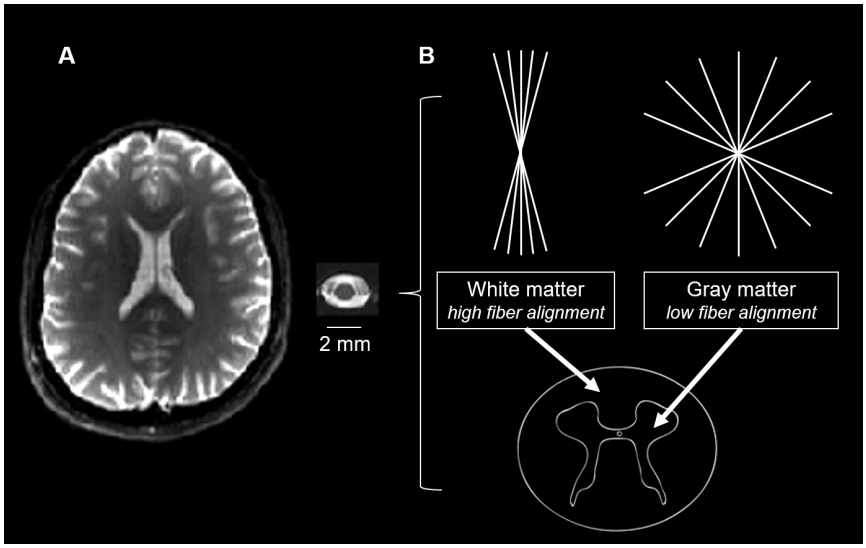

Fig. 5. (A) Illustration of differences in the cross-sectional area between the brain and spinal cord, displaying a single axial slice of the mean T2-weighted (b0) image (refer to Table 4 for details on the datasets). (B) Schematic visualization of the spinal cord, highlighting the "butterfly-shaped" gray matter, which is located in the middle of the spinal cord and contains neuronal cell bodies and loosely aligned fibers, and the surrounding white matter, which contains highly aligned fibers.

Bias in parameters estimates, induced by signal outliers from cardiac, respiratory, and other physiological artifacts, can be mitigated by applying robust fitting as a tensor fitting method (Appendix D.3). Given the higher occurrence of signal outliers in the spinal cord, robust fitting holds particular relevance for spinal cord dMRI. In a previous study, we demonstrated that robust fitting leads to higher FA values within the white matter and lower FA values within the gray matter in spinal cord dMRI data, resulting in an approximately 8% enhancement in contrast-to-noise ratio (Mohammadi et al., 2013). However, it is important to note that robust fitting requires a sufficiently large number of unbiased ("artifact-free") data points; otherwise, it might fail to detect outliers (Chang et al., 2012).

One potential limitation of linearized fitting methods is their operation on logarithmically transformed signals, where the assumption of Gaussian (or Rician) error distribution may not hold. The presence of logarithmically distorted Rician noise distribution not only restricts validity but can also impact the accuracy of the parameter estimates (Andersson, 2008; Chang et al., 2005; Koay et al., 2006), particularly in the low-SNR regime such as in spinal cord dMRI. The WLS and robust fitting algorithms incorporate the signal intensity into the weights of the estimator function (Appendix D.2 and D.3), which was shown to reduce the effect of log-Rician distortion (Salvador et al., 2005). Alternatively, the NLLS algorithm (Appendix D.4) can be used, which circumvents the distortion of the Rician distribution by operating on the original (non-logarithmic) signals, and is therefore expected to yield more accurate parameter estimates, provided that the numerical fitting problem is sufficiently well-conditioned.

In summary, we recommend using robust fitting for dMRI data with a high level of artifacts (frequent outliers), relatively high SNR, and a sufficiently large number of "artifact-free" data points (no outliers). NLLS, especially when combined with Rician bias correction, might be more suitable for dMRI data with lower SNR, such as those acquired for DKI (see Oeschger et al., 2023a for recommended minimum SNR values).

4.2.2 Biophysical diffusion models

Of the biophysical models implemented in ACID, WMTI-Watson rely on DKI metrics (requiring at least two diffusion shells), while NODDI-DTI relies on DTI metrics (requiring a single diffusion shell only). This implies that the challenges associated with the estimation of DTI and DKI metrics, as discussed earlier, also apply to derived biophysical models. Therefore, accurate and precise estimation of DKI and DTI metrics is essential for the successful application of WMTI-Watson and NODDI-DTI, respectively.

For brain dMRI, the DKI-based WMTI-Watson model is typically favored over NODDI-DTI due to the fewer model assumptions, allowing it to better capture diffusion patterns in complex axonal configurations within brain white matter. However, complex models are more "data-hungry" and more susceptible to noise due to the higher number of fitted parameters, which can lead to poorly conditioned optimization problems when the amount and/or the quality of input data are insufficient. Therefore, for low-SNR data, the less complex but better-conditioned NODDI-DTI model might be the preferred choice. On the other hand, NODDI-DTI assumes fixed intra- and extra-cellular diffusivities which are optimized for the brain and might not be valid for the spinal cord. Note that a compromise between these two models could be the WMTI model, which is included as an external tool in ACID (Section 2.8). WMTI which assumes highly aligned fibers, which holds true in white matter regions with high fiber alignment, such as the corpus callosum, but is less appropriate in regions with more complex axonal configurations. The challenges of applying appropriate biophysical models in the spinal cord are further discussed in Appendix H.

Post-mortem and ex vivo neuronal tissues exhibit different diffusivities compared to in vivo tissues due to various factors, including the effect of fixation, changes in chemical properties, and differences in temperature and composition of the embedding fluid. For example, white matter diffusivity was reported to reduce by approximately 85% from in vivo to ex vivo conditions, while the ratio between gray and white matter diffusivities remain similar at around 2-3 (Roebroeck et al., 2019). To accommodate the reduced diffusivities under ex vivo conditions, ACID offers the possibility to adjust the compartmental diffusivities, which act as fixed model parameters, within the NODDI-DTI model. Such an adjustment is not necessary for WMTI and WMTI-Watson, as their compartmental diffusivities are fitted rather than fixed.

4.3 Other considerations

4.3.1 Integration with SPM modules

ACID can be easily combined with SPM tools for segmentation, spatial processing, and voxel-based analysis of parametric maps. Segmenting the brain or spinal cord is often necessary for co-registration, normalization, or tissue specific analyses. In the brain, tissue probability maps of white matter, gray matter, and cerebrospinal fluid can be created by unified segmentation, which is the default segmentation routine in SPM12 (Ashburner & Friston, 2005). A binary brain mask can be generated using the *Make brain mask* utility function (Table 2). To enable SPM's unified segmentation in the spinal cord, the brain tissue priors need to be substituted with the joint brain and spinal cord tissue priors from the probabilistic brain and spinal cord atlas (Blaiotta et al., 2017). However, the atlas only covers the upper cervical cord down to C3; for other spinal levels, the user is referred to automatic (e.g., deepseg (Perone et al., 2018)) or semi-automatic (e.g. active surface method (Horsfield et al., 2010)) segmentation techniques.

Brain dMRI data can be co-registered to the corresponding structural image using *spm_coreg*. For normalizing to the MNI space, we recommend SPM DARTEL (Ashburner, 2007) or Geodesic Shooting (Ashburner & Friston, 2011). As SPM registration tools often rely on brain tissue priors, they cannot be applied directly on spinal cord dMRI. For such data, we recommend the PAM50 template (De Leener et al., 2018) and corresponding normalization tools integrated into the Spinal Cord Toolbox (De Leener et al., 2017).

ACID benefits from SPM's rich statistical framework for voxel-based analysis. SPM's second-level analysis tool (`SPM -> Specify 2nd-level`) performs voxel-based statistical tests on the parametric maps using t-test, ANOVA, or general linear model. In the `SPM -> Results` module, the framework also offers (i) multiple comparison correction in the form of family-wise error rate and false discovery rate, (ii) thresholding the test statistics at cluster- and voxel-level and providing a list of significant clusters/voxels, and (iii) various visualization tools for displaying and saving the significant clusters. Furthermore, ACID's *ROI analysis* utility function (Table 2) can be used to extract mean metrics within subject-specific ROIs in the native space or perform atlas-based analysis in the template space. For atlas-based analysis in the spinal cord, the user is referred to the PAM50 white and gray matter atlas (De Leener et al., 2018).

While brain and spinal cord images are typically analyzed separately, there are scenarios where combining them into a single image can be beneficial. For example, when registering both the brain and spinal cord to a brain-spinal cord template, such as the probabilistic atlas of the brain and spinal cord, the warping field is often obtained using a structural image with a large field of view covering both regions (Fig. 6). To apply this warping field to the brain and spinal cord images, they need to be

fused into a single image. ACID provides the *Fusion* utility function (Table 2) which merges two distinct images, acquired with different FOVs and geometric properties, into a unified large-FOV image (Fig. 6).

Although ACID does not provide tractography or tract-based analysis tools, the output of its model fitting methods can be input into tractography tools such as FSL or the SPM12-based Fibertools (see ACID Wiki for more details).

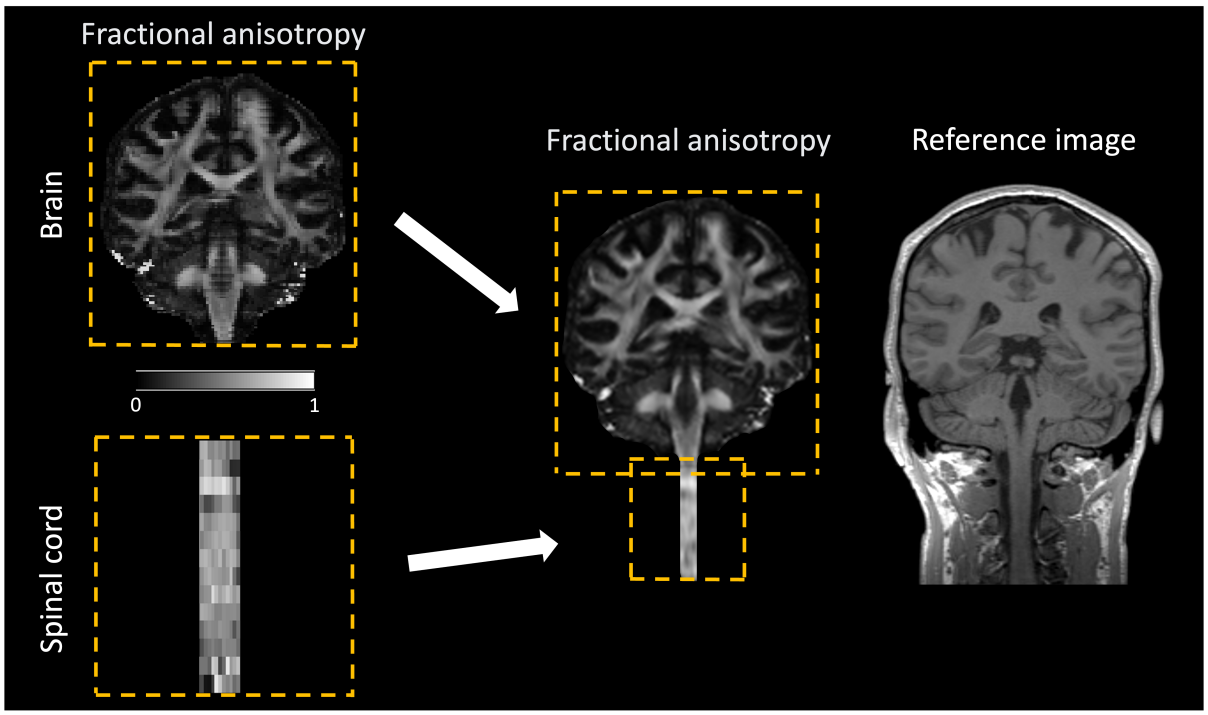

Fig. 6. Merging of two fractional anisotropy (FA) maps, covering the brain and cervical cord, respectively, into a unified FA map using the *Fusion* utility function (Table 2). The two images should ideally share an overlapping region, but they may have different geometric properties such as resolution and number of slices. In the overlapping region, the values are computed as the average of the two underlying images. The merging process requires a structural image for reslicing the images.

4.3.2 Computation time

To speed up the processing and analyzing dMRI data, parallel computing is implemented wherever possible. This technique can significantly accelerate the most time-consuming ACID modules, such as ECMOCO and DTI/DKI fit. Note that parallel computing requires the Parallel Computing Toolbox in MATLAB. Table 6 provides the computation times for selected ACID functions on a typical brain and spinal cord dMRI dataset.

Table 6. Computation times of selected ACID modules on an example in vivo brain and in vivo spinal cord dMRI dataset (refer to Table 4 for details on the datasets), when run on a MacBook M1 laptop (4 cores, 16 GB RAM).

Module	In vivo Brain dMRI	In vivo spinal cord dMRI
ECMOCO	38 min	2 min
msPOAS	7 min	1 min
HySCO	20 min	1 min
RBC	< 1 min	< 1 min
DKI (using NLLS)	27 min	2 min
WMTI-Watson	4 min	1 min

4.3.3 Research applications

ACID has been used in a variety of clinical and neuroscience research, e.g., in dMRI studies assessing cerebral changes in patients with multiple sclerosis (Deppe et al., 2016a, 2016b; Dossi et al., 2018; Kugler & Deppe, 2018) and Parkinson's disease (Szturm et al., 2021), and to assess gliomas (Paschoal et al., 2022; Raja et al., 2016). ACID has also been used to investigate spinal cord white matter following spinal cord injury (David et al., 2019, 2021, 2022; Grabher et al., 2016; Huber et al., 2018; Seif et al., 2020; Vallotton et al., 2021). A non-comprehensive list of studies using the ACID toolbox can be found on the project website[9]. Note that certain ACID functions can be applied to MRI data beyond dMRI as well; for instance, HySCO has been used to correct brain fMRI data for susceptibility artifacts (De Groote et al., 2020). It is important to note that ACID has not been approved for clinical applications by any health agency and it comes with no warranty. Therefore, it should not be used for diagnosis in clinical settings.

4.4 Future directions

The ACID toolbox is the result of a collaborative effort to extend the SPM ecosystem with state-of-the-art processing and modelling tools for dMRI data. Our aim is to make the toolbox widely accessible, leveraging SPM's large and vibrant community. Users can submit their questions, bug reports, and suggestions via the dedicated mailing list or by opening an issue on the git website. This paper provides a snapshot of the toolbox's current state, with several ongoing developments not covered here. The modularity of the toolbox allows for integration of newly developed methods, even when used concurrently with old ones. Biophysical modeling is an emerging field, and we expect many methodological advancements to occur in the coming years. To stay aligned with this development, we aim to continuously incorporate state-of-the art biophysical models into ACID. For ECMOCO, we strive to improve robustness by automatically eliminating voxels with weak signals in the optimization process. If the proportion of voxels with weak signals exceed a critical level, the entire volume will be excluded from estimating the transformation parameters. This feature would offer an unsupervised

[9] http://www.diffusiontools.org/sidebar/studies-using-acid.html

identification of unreliable volumes, as opposed to the current method of manual labelling of slices (see *Exclusion mode* in Appendix A).

5. Conclusion

ACID is an open-source extension to SPM12 that provides a comprehensive framework for processing and analyzing brain, spinal cord, and post-mortem dMRI data. The toolbox was developed to meet the growing demand for spinal cord dMRI studies and research applying biophysical models. ACID leverages the core SPM tools and other SPM extensions, which can be easily integrated into the ACID pipeline.

Acknowledgments

This work was supported by the German Research Foundation (DFG Priority Program 2041 "Computational Connectomics" (MO 2397/5-1, MO 2397/5-2)), the Emmy Noether Stipend (MO 2397/4-1 and 2397/4-2), and the BMBF (01EW1711A and B) in the framework of ERA-NET NEURON. L.R. is supported in part by NSF awards DMS 1751636 and DMS 2038118. P.F. is funded by an SNF Eccellenza Professorial Fellowship grant (PCEFP3_181362/1).

Appendix A. Details on ECMOCO

ECMOCO consists of four steps (Fig. A1):

1. The type of the registration (*slice-wise* or *volume-wise*) and the degrees of freedom (DOF) for the affine transformation are specified by the user.
2. Shell-specific target volumes are generated, and transformation parameters are obtained between all non-diffusion-weighted (b0) volumes and their corresponding targets (Mohammadi et al., 2015a). The parameter iteration for a given b0 volume can be initialized by the transformation parameters of the preceding b0 volume (*initialized registration*, see details below). Only the DOF associated with rigid-body transformation are applied for the b0 volumes, as eddy currents are expected to be negligible for b0 volumes due to the absence of diffusion-sensitizing gradients.
3. Transformation parameters are obtained between all diffusion-weighted (DW) volumes and their corresponding targets. The parameter iteration for a given DW volume can be initialized by the interpolated transformation parameters (rigid-body parameters only) from the b0 volumes (*initialized registration*, see details below).
4. The obtained transformation parameters are applied to reslice all volumes.

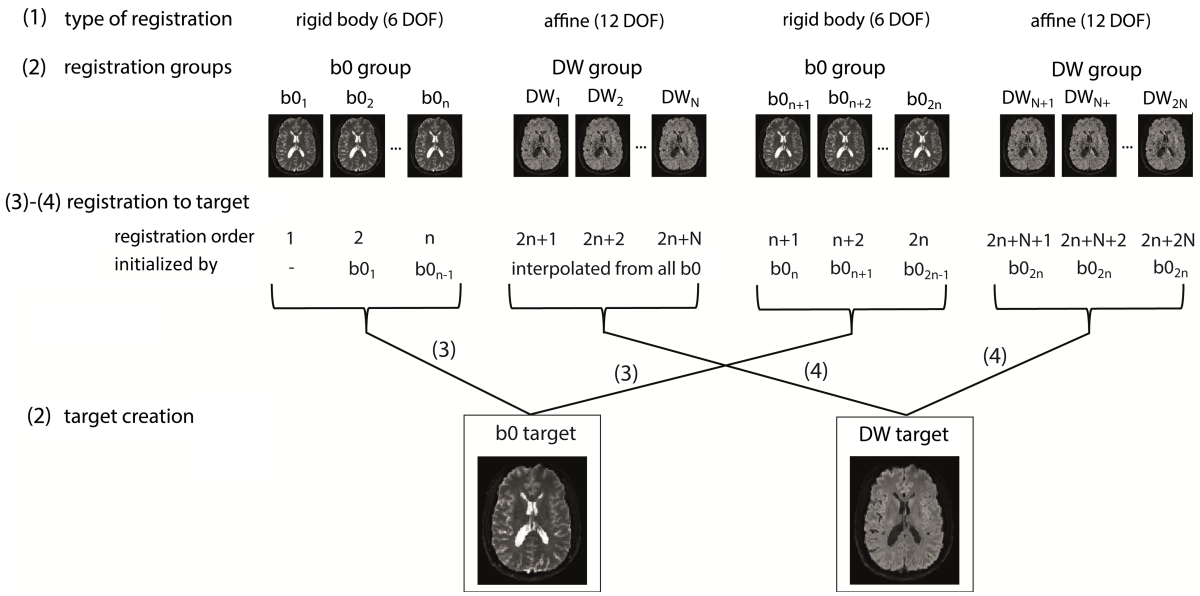

Fig. A1. Registration scheme for an example dMRI dataset, which consists of two sets of non-diffusion-weighted (b0) volumes (n volumes each) and two sets of diffusion-weighted (DW) volumes (N volumes each) interspersed with each other. The b0 and DW volumes form separate registration groups and are registered to their corresponding target volumes. First, the b0 volumes are registered using the rigid-body components of the specified degrees of freedom (DOF), followed by the registration of the DW volumes using all specified DOF. The parameter iteration for a given b0 or DW can be initialized using previously obtained transformation parameters (*initialized registration*).

In addition to *slice-wise* registration, introduced in Section 2.4.1 and demonstrated in Fig. A2, ACID incorporates two additional recent features: *initialized registration* and *exclusion mode*. *Initialized registration* is based on the observation that transformation parameters obtained from high-SNR b0 volumes tend to be more accurate than those obtained from low-SNR DW volumes. With *initialized registration*, the parameter iteration for each b0 volume starts with the transformation parameters obtained from the preceding b0 volume. Once all the b0 volumes have been registered, their transformation parameters are interpolated to the positions of the DW volumes situated between the b0 volumes. Subsequently, the parameter iteration for each DW starts with these interpolated values. If interpolation is not feasible (e.g., the DW volume is situated before the first or after the last b0 volume), the parameter iteration starts with the parameters obtained from the nearest b0 volume. This approach is particularly useful for correcting slow spatial drifts across volumes.

The *exclusion mode* is designed to address volumes with very low SNRs, which can make obtaining reliable transformation parameters difficult. Volumes that are considered not feasible for registration can be identified through visual inspection, e.g., using the *DWI series browser* utility function, and can be inputted into ECMOCO. For these volumes, the rigid-body transformation parameters from the preceding non-excluded volume are applied instead.

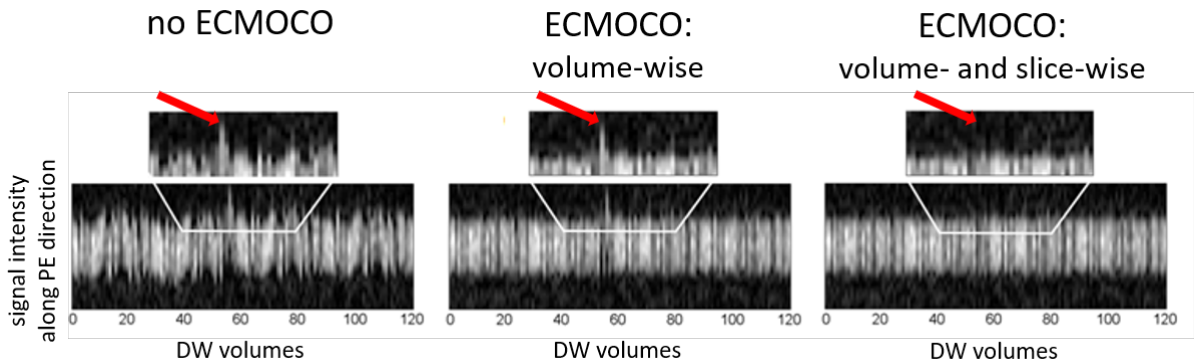

Fig. A2. Qualitative comparison of different motion correction techniques including no correction, volume-wise ECMOCO, and the combination of volume- and slice-wise ECMOCO. The plots show the concatenation of 1D cross-sections along the phase-encoding (PE) direction (anterior-posterior), extracted at fixed x- and z-coordinates from each of the 120 diffusion-weighted (DW) volumes in an in vivo spinal cord dMRI dataset. Additionally, zoomed-in views of a subset of DW volumes are provided to facilitate the assessment of improvements by ECMOCO. Substantial motion along the y-direction was initially observed, which was notably reduced after applying ECMOCO. Importantly, volume-wise ECMOCO did not entirely correct for spatial misalignments in all volumes (an example of failed correction is indicated by the red arrow). Conversely, the combination of volume- and slice-wise ECMOCO effectively corrected spatial misalignments in all DW volumes.

Appendix B. Regions for repeated measures noise estimation method

For optimal denoising (msPOAS, Section 2.4.2) and Rician bias correction (Section 2.4.3), it is crucial to accurately estimate the image noise within the appropriate region of interest. Noise measurements taken from regions outside the body are often suboptimal due to the lower parallelization factor (g-factor) at the edge compared to the center of the field of view. Instead, we recommend estimating the noise according to two distinct scenarios, with each case using the *repeated measures* method (see *Noise estimation* in Table 2). In datasets affected by (temporally varying) physiological artifacts, such as in in vivo brain and spinal cord datasets, we recommend estimating the noise across images with high b-values and within regions where the signal reaches the noise plateau (i.e., within cerebrospinal fluid compartments). For automatic ventricle segmentation within the brain, ACID provides a segmentation batch located at `ACID_TPM/acid-ventricles-batch.m`, which utilizes the *spm_segment* function. In datasets not affected by physiological artifacts, such as in post-mortem dMRI, we recommend estimating the noise across non-diffusion-weighted (b0) images and within either the entire or part of the specimen. Example noise regions are shown in Fig. B1.

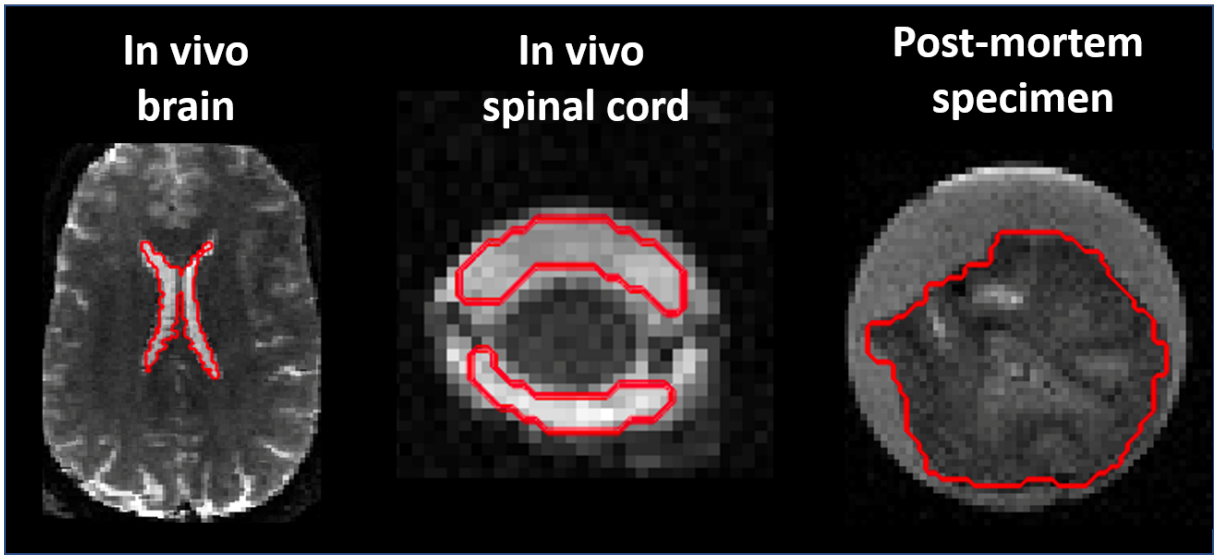

Fig. B1. Non-diffusion-weighted (b0) images of the brain, spinal cord, and a post-mortem specimen, with binary noise masks outlined in red. For the brain and spinal cord, the noise masks encompass areas containing cerebrospinal fluid (CSF), such as the lateral ventricles within the brain and the subarachnoid space within the spinal cord. These masks are considered noise masks for high b-values because the CSF signal, having a high diffusivity, reaches the noise plateau at these high b-values. For the post-mortem specimen, the noise mask encompasses the entire specimen.

Appendix C. Recommendations for adaptive denoising (msPOAS)

If the overall noise reduction is insufficient, *kstar* can be increased at the cost of longer computation time (Tabelow et al., 2015). It is important to note that msPOAS assumes a single global value of *sigma*, which may not always hold. If *sigma* is correctly estimated, the default *lambda* value will ensure optimal adaptation. Incorrect estimation of *sigma* can be compensated by the choice of *lambda*, which makes msPOAS robust against misspecification of *sigma* (Becker et al., 2014). We recommend determining *kappa* automatically based on the number of diffusion directions (Tabelow et al., 2015). However, manual adjustment of *kappa* may be necessary in cases where the SNR is low (e.g., for spinal cord dMRI) or if the dataset has more images with high than with low b-values. The effective number of coils (*ncoils)* is 1 when using SENSE1 reconstructions (Polzehl & Tabelow, 2016; Sotiropoulos et al., 2013), but the correct value is more difficult to determine when using multiple receiver channels for acquisition (Aja-Fernández et al., 2014). It is important to use the same *ncoils* for the estimation of *sigma* and in msPOAS to ensure the same number of degrees of freedom.

Appendix D. Model fitting methods implemented in ACID

Appendix D.1. Ordinary Least Squares

Tensor fitting involves solving the linear regression problem $\boldsymbol{y} = \boldsymbol{B\alpha} + \boldsymbol{\varepsilon}$, where $\boldsymbol{y}$ contains the logarithmic signals, $\boldsymbol{B}$ (b-matrix) contains the gradient directions and strengths, $\boldsymbol{\alpha}$ contains the elements of the diffusion tensor, and $\boldsymbol{\varepsilon}$ contains the model-fit errors (the difference between the actual and fitted signal). The ordinary least squares (OLS) approach employs the estimator function $\rho(\varepsilon_i) = {\varepsilon_i}^2$, where ε_i represents the model-fit error of acquisition i. The solution is obtained by minimizing $\sum_i \varepsilon_i^2$, yielding $\boldsymbol{\alpha_{ols}} = (\boldsymbol{B^T B})^{-1}\boldsymbol{B^T y}$.

Appendix D.2. Weighted Least Squares

The weighted least squares (WLS) approach addresses the heteroscedasticity of the logarithmic data by assigning individual weights to each image in the form of $\omega_i = \hat{S}_i/\sigma_i$, where $\hat{S}_i$ represents the unknown true signal (without noise) and σ_i is the background noise for acquisition i. The estimator function now becomes $\rho(\varepsilon_i) = (\omega_i \varepsilon_i)^2$, yielding the solution $\boldsymbol{\alpha_{wls}} = (\boldsymbol{W^T B^T W B})^{-1}\boldsymbol{W^T B^T W y}$, with $\boldsymbol{W}$ being the diagonal matrix of ω_i. Note that OLS is a special case of WLS, where $\omega_i = 1$ for all i. A practical consideration in obtaining $\boldsymbol{\alpha_{wls}}$ is related to estimating $\hat{S}_i$. One approach is to use the measured noisy signal S_i as an estimate of $\hat{S}_i$. Another approach is to start with the OLS solution and use the fitted signal as an estimate of $\hat{S}_i$, which was shown to be more accurate (Veraart et al., 2013b).

Appendix D.3. Robust fitting

The concept behind robust fitting is to assign lower weights to data points with higher model-fit errors during the fitting process (Mangin et al., 2002). The robust fitting method implemented in ACID (Mohammadi et al., 2013) is based on the "Patching ArTefacts from Cardiac and Head motion" (PATCH) technique (Zwiers, 2010). While the form of the estimator function is similar to that of WLS, PATCH factorizes the weighting function into a product of dedicated weighting functions. Specifically, ω_i is factorized into three components as $\omega_i = \omega_{i1}\omega_{i2}\omega_{i3}$, where each component is designed to address different types of artifacts: ω_{i1} and ω_{i2} account for regional and slice-wise artifacts, respectively, while ω_{i3} is the same as the weight term in WLS. ω_{i1} and ω_{i2} are exponentially decaying functions of ε_i: $\omega_{i1} = \exp\left(-\left[\frac{A_1\varepsilon_i}{C_1}\right]^2\right)$, $\omega_{i2} = \exp\left(-\left[\frac{A_2\varepsilon_{i,sl}}{C_2}\right]^2\right)$, where $\varepsilon_{i,sl} = \sum_{k=1}^{n}\frac{\varepsilon_{ik}}{\sqrt{n}}$ is the slice-average model-fit error, with n being the number of voxels in the slice. A_1 and A_2 are model parameters, by default set to 0.3 and 0.1, respectively, with higher values resulting in a faster exponential decay. C_1 and C_2 are estimates of the standard deviation of ε_i and $\varepsilon_{i,sl}$, respectively, in the absence of outliers, and are computed as $C_1 = 1.4826 \cdot \mathrm{median}(|\varepsilon_i|)$, $C_2 = 1.4826 \cdot \mathrm{median}(|\varepsilon_{i,sl}|)$ (Hampel, 1974; Rousseeuw & Croux, 1993). Note that accurate estimation of C_1 and C_2 is crucial for effectively downweighing outliers. This holds true as long as outliers are sparsely distributed and the median of the model-fit errors remains unaffected. However, frequent occurrence of outliers can increase C, resulting in less efficient downweighing of outliers. While OLS and WLS independently fit the tensor in each voxel, PATCH makes use of the observation that physiological noise represents a structured, spatially correlated noise. To accommodate the anticipated smoothness of C_1, the median operator is spatially smoothed using a 2D Gaussian kernel before computing C_1 (Zwiers, 2010).

As a modification to PATCH, the robust fitting method incorporates Tikhonov regularization to handle ill-conditioned weighting matrices resulting from a high occurrence of outliers. This leads to the solution $\boldsymbol{\alpha_\lambda} = [\boldsymbol{W^T B^T W B} + \lambda \boldsymbol{B^T B}]^{-1}\boldsymbol{W^T B^T W y}$, where $\boldsymbol{W}$ represents the diagonal matrix of factorized weights, and λ is the Tikhonov regularization factor. λ must be carefully chosen as a trade-off since too low values fail to eliminate ill-conditioning, whereas too high values result in bias in the estimated parameters. The above equation cannot be solved readily, as $\boldsymbol{W}$ is a function of $\boldsymbol{\varepsilon}$, which is only available after obtaining the solution. This is addressed by using an iteratively re-weighted least squares (IRLS) algorithm. In the first iteration, ω_i is set to 1 for all i to obtain the OLS solution $\boldsymbol{\alpha_{ols}}$, and to calculate the initial $\boldsymbol{\varepsilon}$. In the second iteration, an updated $\boldsymbol{W}$ is computed based on the initial $\boldsymbol{\varepsilon}$, which is then used to compute $\boldsymbol{\alpha_\lambda}$. In each further iteration, $\boldsymbol{\varepsilon}$ from the preceding iteration is used to update $\boldsymbol{W}$, which is in turn used to compute the updated $\boldsymbol{\alpha_\lambda}$. This iterative process is repeated until convergence or until the predefined number of iterations is exceeded.

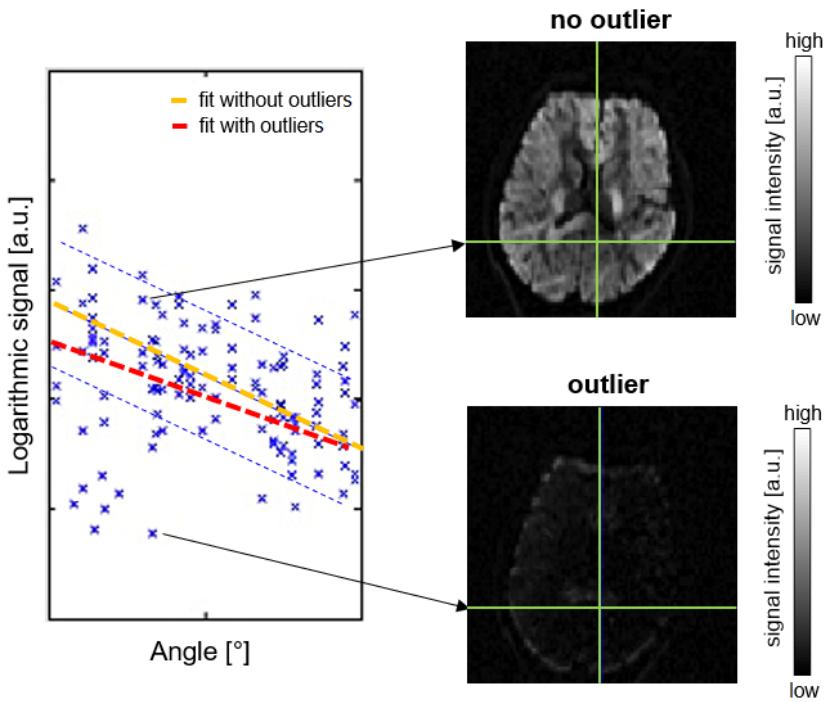

Fig. D1. Schematic illustration of how robust fitting downweighs outliers in the model fit. The scatter plot displays the signal intensities against the angle of the diffusion gradient (bvec) in a particular voxel. The confidence interval of the data points is indicated as blue dashed lines. The voxels corresponding to two selected data points, one inside (upper arrow) and another far outside the confidence interval ("outlier", lower arrow), are indicated by green crosshairs in the axial slices on the right. During the model fit, a linear curve is fitted on the logarithmic signal intensities. The presence of outlier data points leads to a biased model fit (red dashed line) and hence to biased tensor estimates when using ordinary least squares (OLS) model fitting. In contrast, robust fitting downweighs the influence of outliers, leading to a more robust model fit (yellow dashed line).

Appendix D.4. Non-linear least squares

The non-linear least squares (NLLS) method solves the optimization problem $\underline{\boldsymbol{\alpha}}_{\boldsymbol{nlls}} = \underset{\underline{\boldsymbol{\alpha}}}{\operatorname{argmin}} \sum_i \left(S_{b,\overrightarrow{g_i}} - f(\alpha)\right)^2$, where f represents the signal model (DTI or DKI), α the model parameters (elements of the diffusion and/or kurtosis tensors), and $S_{b,\overrightarrow{g_i}}$ the measured signal intensities for a specific diffusion weighting b and diffusion gradient direction $\overrightarrow{g_i}$. The NLLS optimization problem is solved with a Gauss-Newton algorithm.

Appendix E. Example diagnostic plots

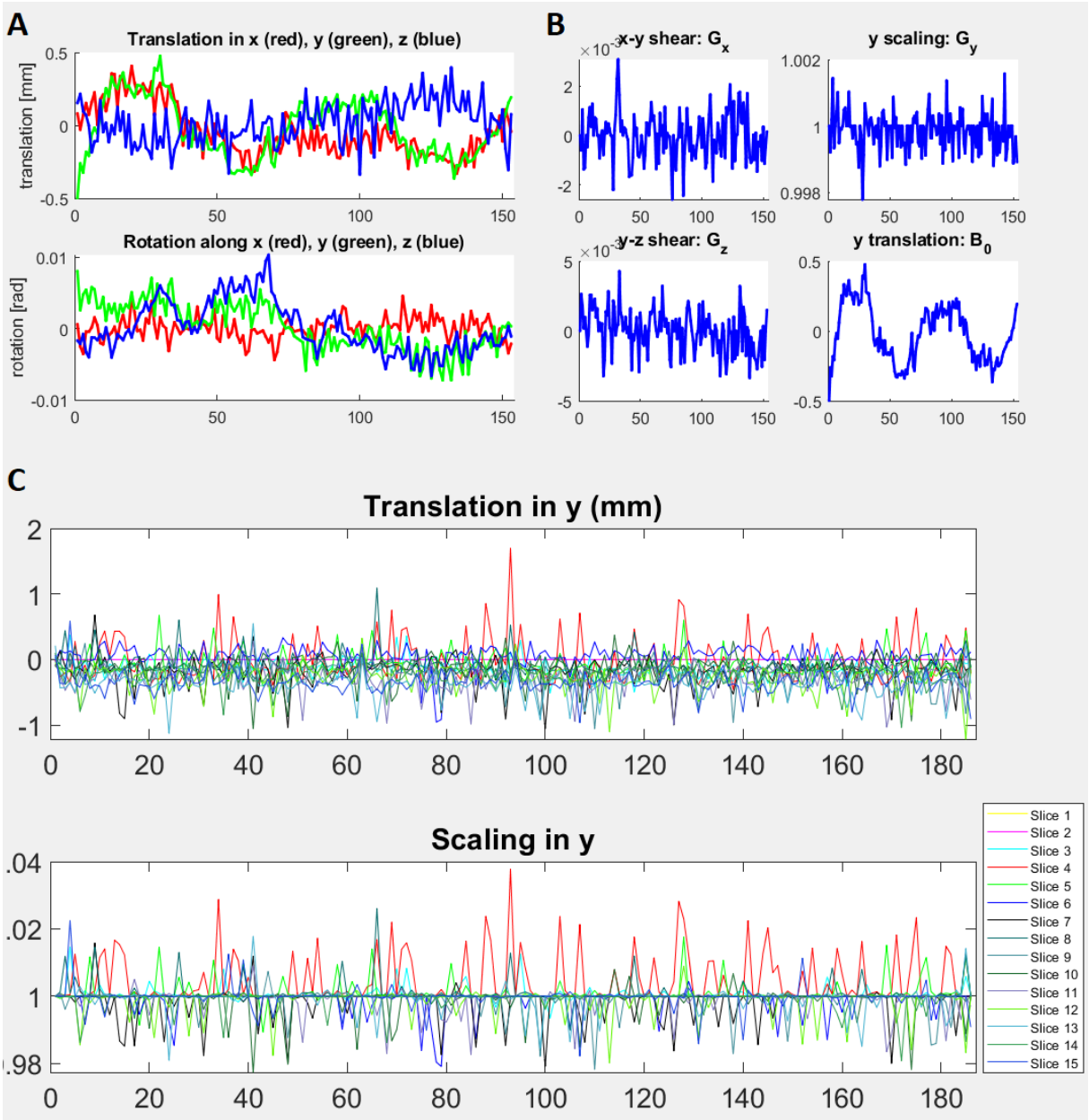

Fig. E1. Diagnostic plots, optionally generated by ECMOCO, displaying the transformation parameters for all volumes (in the case of volume-wise registration) or slices (in the case of slice-wise registration). In volume-wise registration, demonstrated here with an in vivo brain dMRI dataset, two figures are created to plot the transformation parameters associated with motion (A) and eddy-current-related displacements (B). In slice-wise registration, shown here with an in vivo spinal cord dMRI dataset, a single figure is created to plot the transformation parameters with separate subfigures for each estimated degree of freedom (B). Excessive displacements in volumes/slices indicate either extreme movements, eddy-current artifacts, or a failed estimation of transformation parameters.

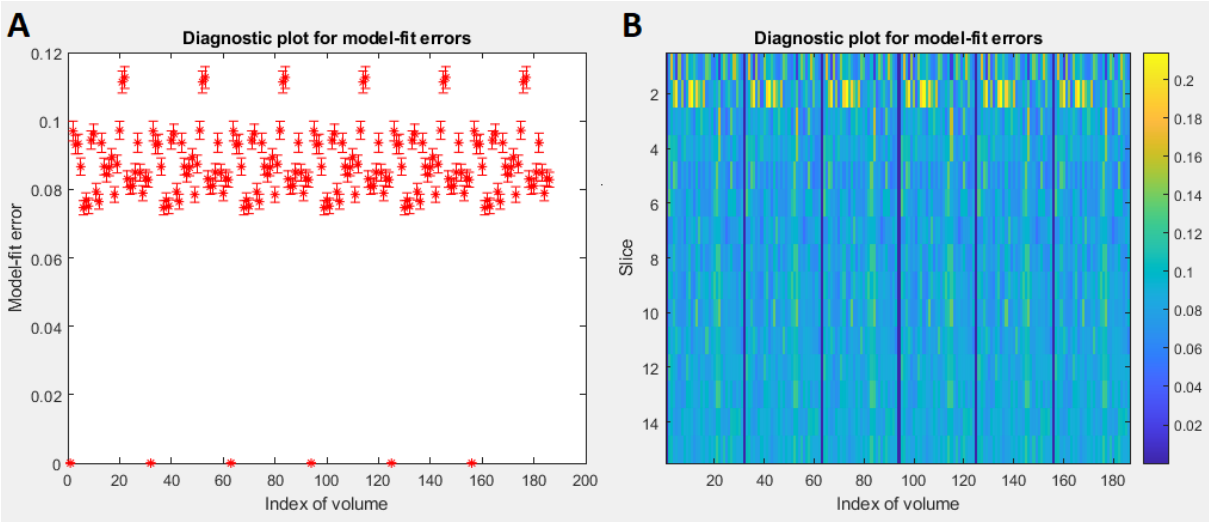

Fig. E2. Diagnostic plots, optionally generated by the *Diffusion tensor/kurtosis imaging* module, displaying the average (logarithmic) model-fit error within the provided mask of the region of interest for each volume and slice, demonstrated here with an in vivo spinal cord dataset and a spinal cord mask. Volumes/slices with high model-fit error (outliers) indicate a significant number of corrupted volumes (e.g., due to misregistration, physiological, or other artifacts) or an inadequate model for capturing the underlying complexity of diffusion. Here, periodically occurring pairs of volumes with high model-fit errors are the result of an inadequate model fit due to the low signal-to-noise ratio caused by the diffusion-sensitizing gradient aligned parallel to the spinal cord (A). Also notice that model-fit error is the highest within slice 2, which could be due to more physiological artifacts in that location. For an even more precise diagnosis of signal outliers, the voxel-wise root-mean-square of the model-fit error map (suffix: RMSE-LOG_map.nii) or the 4D model-fit error map (suffix: ERROR-LOG_map.nii) can be visually inspected to help identify individual outlier voxels or data points, respectively.

Appendix F. Kurtosis bias

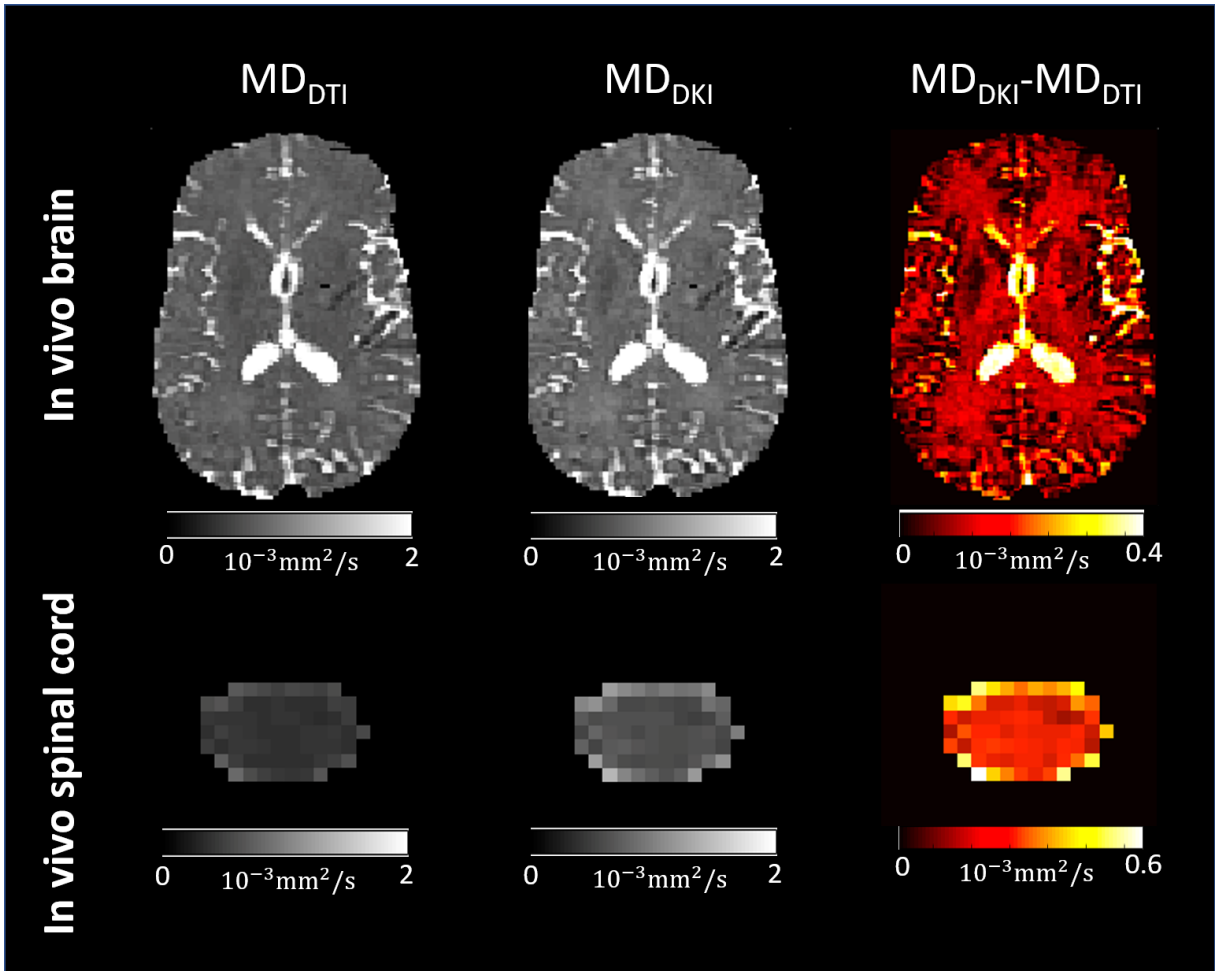

Fig. F1. Kurtosis bias in the mean diffusivity (MD) maps in an in vivo brain and in vivo spinal cord dataset (refer to Table 4 for details on the datasets). This bias, shown in the right column, refers to the difference in the estimated diffusivity values when using the lower diffusion shells only ($\mathrm{MD_{DTI}}$, tensor model, left column) or both the lower and higher diffusion shells ($\mathrm{MD_{DKI}}$, kurtosis model, middle column). On average, the kurtosis bias was 12% and 54% within the brain white matter and spinal cord, respectively.

Appendix G. Effect of artifact correction on diffusion kurtosis estimates

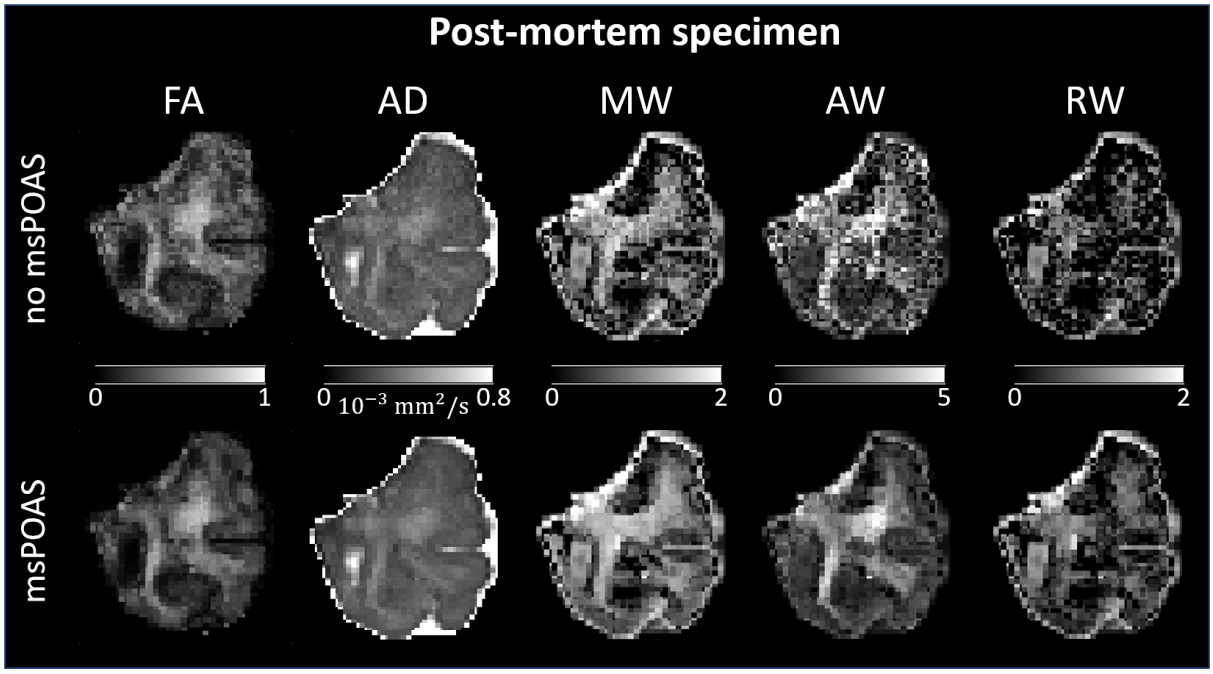

Fig. G1. Comparison between maps of fractional anisotropy (FA), axial diffusivity (AD), mean of the kurtosis tensor (MW), axial kurtosis (AW), and radial kurtosis (RW) with and without applying adaptive denoising (msPOAS). The msPOAS-corrected maps appear less noisy while preserving tissue edges.

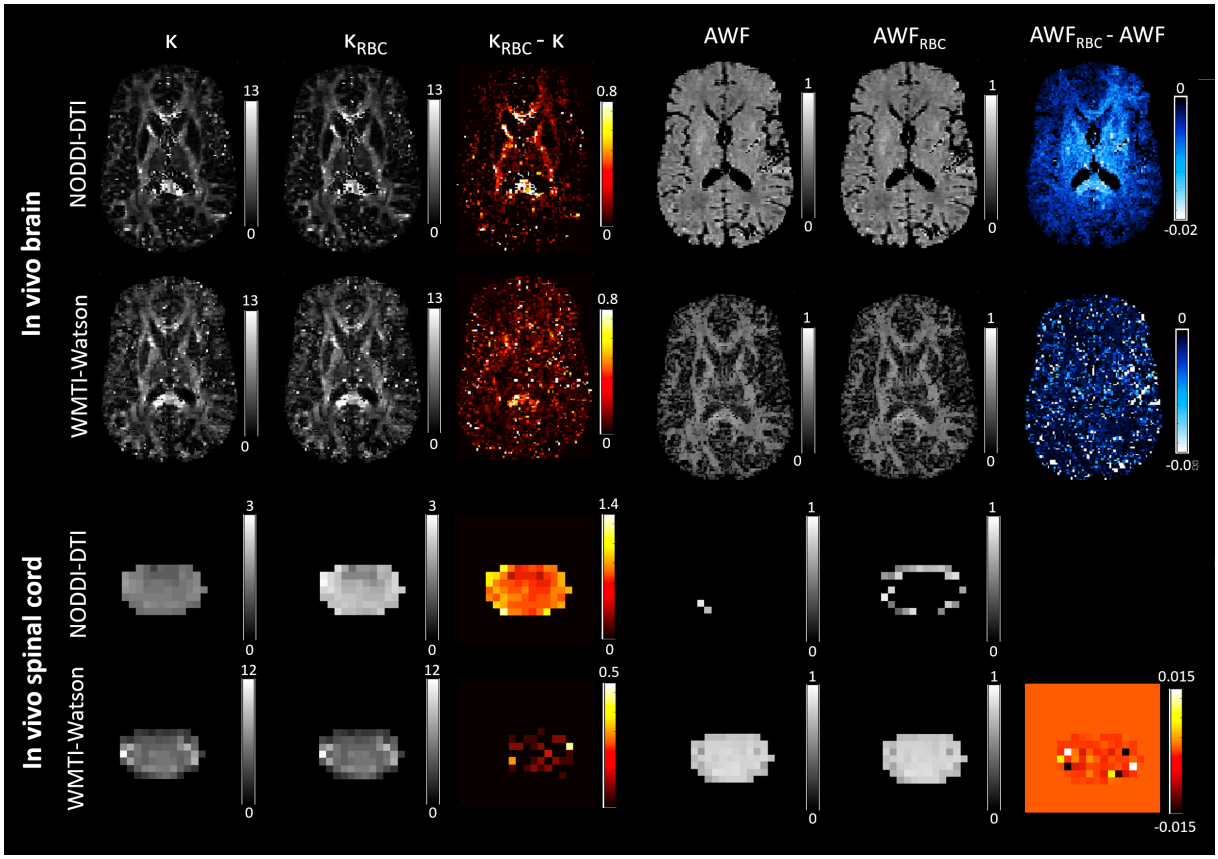

Fig. G2. The influence of Rician bias correction (RBC) on maps of biophysical parameter estimates, derived from the NODDI-DTI and WMTI-Watson model, including axon orientation dispersion (κ), in an in vivo brain and spinal cord dataset (refer to Table 4 for details on the datasets). These maps were computed without (left column) and with (middle column) RBC; their voxel-wise difference, known as the Rician bias, is shown in the right column. RBC slightly decreased the mean of the kurtosis tensor both in the brain and spinal cord, which resulted in an increase in κ. The estimation of AWF was not feasible using the NODDI-DTI model, as the DTI-derived MD values fell below the range in which the NODDI-DTI model provides a valid representation (Equation (4) in Edwards et al., 2017). This could be attributed to either the underestimation of MD due to the kurtosis bias (Appendix F), or the invalidity of fixed compartmental diffusivities in the NODDI-DTI model.

Appendix H. Biophysical parameters in the brain and spinal cord

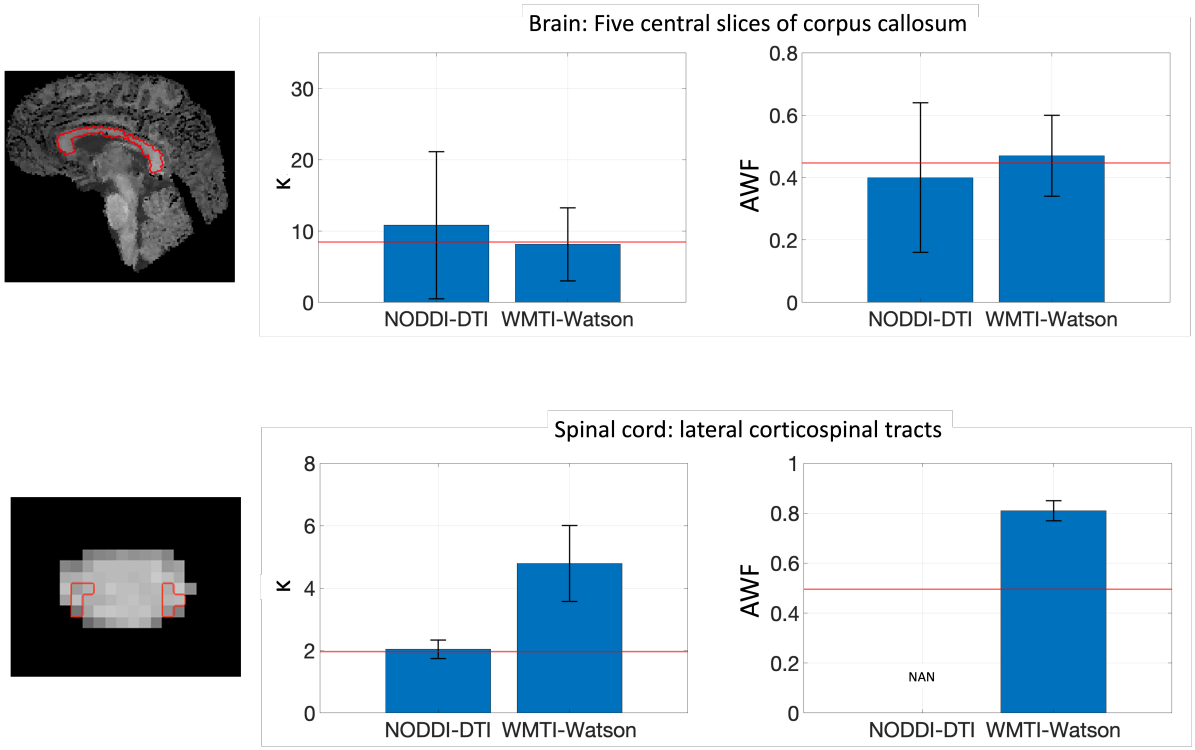

Fig. H1. Bar plots displaying the neurite orientation dispersion (κ) and axonal water fraction (AWF) within the five central slices of the corpus callosum and the lateral corticospinal tracts in the spinal cord. The corpus callosum was manually segmented, while the lateral corticospinal tracts were segmented using the PAM50 spinal cord white matter atlas. The red horizontal lines represent literature values. Orientation dispersion index values reported in the literature were converted to κ as per Equation (1) in (Mollink et al., 2017). Within the corpus callosum, the κ values were (mean ± std) 10.8 □ 10.3 and 8.1 □ 5.1 when derived from the NODDI-DTI (single shell) and WMTI-Watson model (two shells), respectively, which fall within the range of literature values obtained post-mortem using polarized light imaging (Mollink et al., 2017). The AWF values derived from NODDI-DTI (0.40 □ 0.25) and WMTI-Watson model (0.47 □ 0.13) were also similar to literature values obtained using WMTI (Margoni et al., 2019). Within the lateral corticospinal tracts, the κ values derived from NODDI-DTI were notably lower than those derived from WMTI-Watson (2.0 □ 0.3 vs. 4.79 □ 1.22) and were in agreement with literature values obtained post-mortem by NODDI (Grussu et al., 2017). The AWF values were 0.82 □ 0.04 when derived from the WMTI-Watson model, which were substantially higher than literature values obtained using AxCaliber diffusion data (Duval et al., 2015). The estimation of AWF was not feasible using the NODDI-DTI model, as the DTI-derived MD values fell below the range in which the NODDI-DTI model provides a valid representation (see Equation (4) in Edwards et al., 2017). This could be attributed to either the underestimation of MD due to the kurtosis bias (Appendix F), or the invalidity of fixed compartmental diffusivities in the NODDI-DTI model.

References

Ades-Aron, B., Veraart, J., Kochunov, P., McGuire, S., Sherman, P., Kellner, E., Novikov, D. S., & Fieremans, E. (2018). Evaluation of the accuracy and precision of the diffusion parameter EStImation with Gibbs and NoisE removal pipeline. *NeuroImage*, *183*, 532–543. https://doi.org/10.1016/j.neuroimage.2018.07.066

Aja-Fernández, S., Vegas-Sánchez-Ferrero, G., & Tristán-Vega, A. (2014). Noise estimation in parallel MRI: GRAPPA and SENSE. *Magnetic Resonance Imaging*, *32*(3), 281–290. https://doi.org/10.1016/j.mri.2013.12.001

Alexander, D. C., Dyrby, T. B., Nilsson, M., & Zhang, H. (2019). Imaging brain microstructure with diffusion MRI: practicality and applications. *NMR in Biomedicine*, *32*(4), e3841. https://doi.org/10.1002/nbm.3841

Andersson, J. L. R. (2008). Maximum a posteriori estimation of diffusion tensor parameters using a Rician noise model: Why, how and but. *NeuroImage*, *42*(4), 1340–1356. https://doi.org/10.1016/j.neuroimage.2008.05.053

Andersson, J. L. R., & Sotiropoulos, S. N. (2016). An integrated approach to correction for off-resonance effects and subject movement in diffusion MR imaging. *NeuroImage*, *125*, 1063–1078. https://doi.org/10.1016/j.neuroimage.2015.10.019

André, E. D., Grinberg, F., Farrher, E., Maximov, I. I., Shah, N. J., Meyer, C., Jaspar, M., Muto, V., Phillips, C., & Balteau, E. (2014). Influence of noise correction on intra- and inter-subject variability of quantitative metrics in diffusion kurtosis imaging. *PLoS ONE*, *9*(4). https://doi.org/10.1371/journal.pone.0094531

Ashburner, J. (2007). A fast diffeomorphic image registration algorithm. *NeuroImage*, *38*(1), 95–113. https://doi.org/10.1016/j.neuroimage.2007.07.007

Ashburner, J., & Friston, K. J. (2005). Unified segmentation. *NeuroImage*, *26*(3), 839–851. https://doi.org/10.1016/j.neuroimage.2005.02.018

Ashburner, J., & Friston, K. J. (2011). Diffeomorphic registration using geodesic shooting and Gauss-Newton optimisation. *NeuroImage*, *55*(3), 954–967. https://doi.org/10.1016/j.neuroimage.2010.12.049

Barker, G. J. (2001). Diffusion-weighted imaging of the spinal cord and optic nerve. *Journal of the Neurological Sciences*, *186*, 45–49. https://doi.org/10.1016/S0022-510X(01)00490-7

Basser, P. J., Mattiello, J., & LeBihan, D. (1994). Estimation of the effective self-diffusion tensor from the NMR spin echo. *Journal of Magnetic Resonance, Series B*, *103*(3), 247–254. https://doi.org/10.1006/jmrb.1994.1037

Basser, P. J., & Pajevic, S. (2000). Statistical artifacts in diffusion tensor MRI (DT-MRI) caused by background noise. *Magnetic Resonance in Medicine*, *44*(1), 41–50. https://doi.org/10.1002/1522-2594(200007)44:1<41::AID-MRM8>3.0.CO;2-O

Becker, S. M. A., Tabelow, K., Mohammadi, S., Weiskopf, N., & Polzehl, J. (2014). Adaptive smoothing of multi-shell diffusion weighted magnetic resonance data by msPOAS. *NeuroImage*, *95*, 90–105. https://doi.org/10.1016/j.neuroimage.2014.03.053

Becker, S. M. A., Tabelow, K., Voss, H. U., Anwander, A., Heidemann, R. M., & Polzehl, J. (2012). Position-orientation adaptive smoothing of diffusion weighted magnetic resonance data (POAS). *Medical Image Analysis*, *16*(6), 1142–1155. https://doi.org/10.1016/j.media.2012.05.007

Blaiotta, C., Freund, P., Cardoso, M. J., & Ashburner, J. (2017). Generative diffeomorphic atlas construction from brain and spinal cord MRI data. *ArXiv*. http://arxiv.org/abs/1707.01342

Callaghan, P. T., Eccles, C. D., & Xia, Y. (1988). NMR microscopy of dynamic displacements: K-space and q-space imaging. *Journal of Physics E: Scientific Instruments*, *21*(8), 820–822. https://doi.org/10.1088/0022-3735/21/8/017

Chang, L. C., Jones, D. K., & Pierpaoli, C. (2005). RESTORE: Robust estimation of tensors by outlier rejection. *Magnetic Resonance in Medicine*, *53*(5), 1088–1095. https://doi.org/10.1002/mrm.20426

Chang, L. C., Walker, L., & Pierpaoli, C. (2012). Informed RESTORE: A method for robust estimation of

diffusion tensor from low redundancy datasets in the presence of physiological noise artifacts. *Magnetic Resonance in Medicine*, *68*(5), 1654–1663. https://doi.org/10.1002/mrm.24173

Chun, S. Y., Li, K. C., Xuan, Y., Xun, M. J., & Qin, W. (2005). Diffusion tensor tractography in patients with cerebral tumors: A helpful technique for neurosurgical planning and postoperative assessment. *European Journal of Radiology*, *56*(2), 197–204. https://doi.org/10.1016/j.ejrad.2005.04.010

Clark, I. A., Callaghan, M. F., Weiskopf, N., Maguire, E. A., & Mohammadi, S. (2021). Reducing Susceptibility Distortion Related Image Blurring in Diffusion MRI EPI Data. *Frontiers in Neuroscience*, *15*, 955. https://doi.org/10.3389/fnins.2021.706473

Coelho, S., Baete, S. H., Lemberskiy, G., Ades-Aron, B., Barrol, G., Veraart, J., Novikov, D. S., & Fieremans, E. (2022). Reproducibility of the Standard Model of diffusion in white matter on clinical MRI systems. *NeuroImage*, *257*, 119290. https://doi.org/10.1016/j.neuroimage.2022.119290

Cohen-Adad, J., Rossignol, S., & Hoge, R. (2009). Slice-by-slice motion correction in spinal cord fMRI: SliceCorr. *Proceedings of the 17th Scientific Meeting, International Society for Magnetic Resonance in Medicine, Honolulu, USA*, 3181.

Cohen, Y., Anaby, D., & Morozov, D. (2017). Diffusion MRI of the spinal cord: from structural studies to pathology. *NMR in Biomedicine*, *30*(3). https://doi.org/10.1002/nbm.3592

Constantinides, C. D., Atalar, E., & McVeigh, E. (1997). Signal-to-noise measurements in magnitude images from NMR phased arrays. *Proceedings of the Annual International Conference of the IEEE Engineering in Medicine and Biology*, *1*, 456–459. https://doi.org/10.1109/iembs.1997.754578

David, G., Freund, P., & Mohammadi, S. (2017). The efficiency of retrospective artifact correction methods in improving the statistical power of between-group differences in spinal cord DTI. *NeuroImage*, *158*, 296–307. https://doi.org/10.1016/j.neuroimage.2017.06.051

David, G., Pfyffer, D., Vallotton, K., Pfender, N., Thompson, A., Weiskopf, N., Mohammadi, S., Curt, A., & Freund, P. (2021). Longitudinal changes of spinal cord grey and white matter following spinal cord injury. *Journal of Neurology, Neurosurgery and Psychiatry*, *92*, 1222–1230. https://doi.org/10.1136/jnnp-2021-326337

David, G., Seif, M., Huber, E., Hupp, M., Rosner, J., Dietz, V., Weiskopf, N., Mohammadi, S., & Freund, P. (2019). In vivo evidence of remote neural degeneration in the lumbar enlargement after cervical injury. *Neurology*, *92*(12), E1367–E1377. https://doi.org/10.1212/WNL.0000000000007137

David, G., Vallotton, K., Hupp, M., Curt, A., Freund, P., & Seif, M. (2022). Extent of cord pathology in the lumbosacral enlargement in non-traumatic versus traumatic spinal cord injury. *Journal of Neurotrauma*, *39*(9–10), 639–650. https://doi.org/10.1089/neu.2021.0389

De Groote, S., Goudman, L., Peeters, R., Linderoth, B., Vanschuerbeek, P., Sunaert, S., De Jaeger, M., De Smedt, A., & Moens, M. (2020). Magnetic resonance imaging exploration of the human brain during 10 kHz spinal cord stimulation for failed back surgery syndrome: A resting state functional magnetic resonance imaging study. *Neuromodulation*, *23*(1), 46–55. https://doi.org/10.1111/ner.12954

De Leener, B., Fonov, V. S., Collins, D. L., Callot, V., Stikov, N., & Cohen-Adad, J. (2018). PAM50: Unbiased multimodal template of the brainstem and spinal cord aligned with the ICBM152 space. *NeuroImage*, *165*, 170–179. https://doi.org/10.1016/j.neuroimage.2017.10.041

De Leener, B., Lévy, S., Dupont, S. M., Fonov, V. S., Stikov, N., Collins, D. L., Callot, V., & Cohen-Adad, J. (2017). SCT: Spinal Cord Toolbox, an open-source software for processing spinal cord MRI data. *NeuroImage*, *145*, 24–43. https://doi.org/10.1016/j.neuroimage.2016.10.009

Deppe, M., Krämer, J., Tenberge, J. G., Marinell, J., Schwindt, W., Deppe, K., Groppa, S., Wiendl, H., & Meuth, S. G. (2016a). Early silent microstructural degeneration and atrophy of the thalamocortical network in multiple sclerosis. *Human Brain Mapping*, *37*(5), 1866–1879. https://doi.org/10.1002/hbm.23144

Deppe, M., Tabelow, K., Krämer, J., Tenberge, J. G., Schiffler, P., Bittner, S., Schwindt, W., Zipp, F., Wiendl, H., & Meuth, S. G. (2016b). Evidence for early, non-lesional cerebellar damage in

patients with multiple sclerosis: DTI measures correlate with disability, atrophy, and disease duration. *Multiple Sclerosis*, *22*(1), 73–84. https://doi.org/10.1177/1352458515579439

Dietrich, O., Raya, J. G., Reeder, S. B., Reiser, M. F., & Schoenberg, S. O. (2007). Measurement of signal-to-noise ratios in MR images: Influence of multichannel coils, parallel imaging, and reconstruction filters. *Journal of Magnetic Resonance Imaging*, *26*(2), 375–385. https://doi.org/10.1002/jmri.20969

Dossi, D. E., Chaves, H., Heck, E. S., Murúa, S. R., Ventrice, F., Bakshi, R., Quintana, F. J., Correale, J., & Farez, M. F. (2018). Effects of systolic blood pressure on brain integrity in multiple sclerosis. *Frontiers in Neurology*, *9*, 487. https://doi.org/10.3389/fneur.2018.00487

Draganski, B., Ashburner, J., Hutton, C., Kherif, F., Frackowiak, R. S. J., Helms, G., & Weiskopf, N. (2011). Regional specificity of MRI contrast parameter changes in normal ageing revealed by voxel-based quantification (VBQ). *NeuroImage*, *55*(4), 1423–1434. https://doi.org/10.1016/j.neuroimage.2011.01.052

Dubois, J., Dehaene-Lambertz, G., Kulikova, S., Poupon, C., Hüppi, P. S., & Hertz-Pannier, L. (2014). The early development of brain white matter: A review of imaging studies in fetuses, newborns and infants. *Neuroscience*, *276*, 48–71. https://doi.org/10.1016/j.neuroscience.2013.12.044

Duval, T., McNab, J. A., Setsompop, K., Witzel, T., Schneider, T., Huang, S. Y., Keil, B., Klawiter, E. C., Wald, L. L., & Cohen-Adad, J. (2015). In vivo mapping of human spinal cord microstructure at 300mT/m. *NeuroImage*, *118*, 494–507. https://doi.org/10.1016/j.neuroimage.2015.06.038

Edwards, L. J., Pine, K. J., Ellerbrock, I., Weiskopf, N., & Mohammadi, S. (2017). NODDI-DTI: Estimating neurite orientation and dispersion parameters from a diffusion tensor in healthy white matter. *Frontiers in Neuroscience*, *11*, 720. https://doi.org/10.3389/fnins.2017.00720

Farbota, K. D., Bendlin, B. B., Alexander, A. L., Rowley, H. A., Dempsey, R. J., & Johnson, S. C. (2012). Longitudinal diffusion tensor imaging and neuropsychological correlates in traumatic brain injury patients. *Frontiers in Human Neuroscience*, *6*, 1–15. https://doi.org/10.3389/fnhum.2012.00160

Fieremans, E., Jensen, J. H., & Helpern, J. A. (2011). White matter characterization with diffusional kurtosis imaging. *NeuroImage*, *58*(1), 177–188. https://doi.org/10.1016/j.neuroimage.2011.06.006

Friston, K. J., & Ashburner, J. (1997). Multimodal image coregistration and partitioning—a unified framework. *NeuroImage*, *6*(3), 209–217. https://doi.org/10.1006/nimg.1997.0290

Garyfallidis, E., Brett, M., Amirbekian, B., Rokem, A., van der Walt, S., Descoteaux, M., & Nimmo-Smith, I. (2014). Dipy, a library for the analysis of diffusion MRI data. *Frontiers in Neuroinformatics*, *8*, 8. https://doi.org/10.3389/fninf.2014.00008

Gerstner, E. R., & Sorensen, A. G. (2011). Diffusion and diffusion tensor imaging in brain cancer. *Seminars in Radiation Oncology*, *21*(2), 141–146. https://doi.org/10.1016/j.semradonc.2010.10.005

Gorgolewski, K. J., Auer, T., Calhoun, V. D., Craddock, R. C., Das, S., Duff, E. P., Flandin, G., Ghosh, S. S., Glatard, T., Halchenko, Y. O., Handwerker, D. A., Hanke, M., Keator, D., Li, X., Michael, Z., Maumet, C., Nichols, B. N., Nichols, T. E., Pellman, J., … Poldrack, R. A. (2016). The brain imaging data structure, a format for organizing and describing outputs of neuroimaging experiments. *Scientific Data*, *3*(1), 1–9. https://doi.org/10.1038/sdata.2016.44

Grabher, P., Mohammadi, S., Trachsler, A., Friedl, S., David, G., Sutter, R., Weiskopf, N., Thompson, A. J., Curt, A., & Freund, P. (2016). Voxel-based analysis of grey and white matter degeneration in cervical spondylotic myelopathy. *Scientific Reports*, *6*(1), 1–10. https://doi.org/10.1038/srep24636

Grussu, F., Schneider, T., Tur, C., Yates, R. L., Tachrount, M., Ianuş, A., Yiannakas, M. C., Newcombe, J., Zhang, H., Alexander, D. C., DeLuca, G. C., & Gandini Wheeler-Kingshott, C. A. M. (2017). Neurite dispersion: a new marker of multiple sclerosis spinal cord pathology? *Annals of Clinical and Translational Neurology*, *4*(9), 663–679. https://doi.org/10.1002/acn3.445

Gu, X., & Eklund, A. (2019). Evaluation of six phase encoding based susceptibility distortion correction methods for diffusion MRI. *Frontiers in Neuroinformatics*, *13*, 76. https://doi.org/10.3389/fninf.2019.00076

Gudbjartsson, H., & Patz, S. (1995). The rician distribution of noisy mri data. *Magnetic Resonance in Medicine*, *34*(6), 910–914. https://doi.org/10.1002/mrm.1910340618

Hampel, F. R. (1974). The Influence Curve and Its Role in Robust Estimation. *Journal of the American Statistical Association*, *69*(346), 383. https://doi.org/10.2307/2285666

Hansen, B., Shemesh, N., & Jespersen, S. N. (2016). Fast imaging of mean, axial and radial diffusion kurtosis. *NeuroImage*, *142*, 381–393. https://doi.org/10.1016/j.neuroimage.2016.08.022

Horsfield, M. A., Lai, M., Webb, S. L., Barker, G. J., Tofts, P. S., Turner, R., Rudge, P., & Miller, D. H. (1996). Apparent diffusion coefficients in benign and secondary progressive multiple sclerosis by nuclear magnetic resonance. *Magnetic Resonance in Medicine*, *36*(3), 393–400. https://doi.org/10.1002/mrm.1910360310

Horsfield, M. A., Sala, S., Neema, M., Absinta, M., Bakshi, A., Sormani, M. P., Rocca, M. A., Bakshi, R., & Filippi, M. (2010). Rapid semi-automatic segmentation of the spinal cord from magnetic resonance images: Application in multiple sclerosis. *NeuroImage*, *50*(2), 446–455. https://doi.org/10.1016/j.neuroimage.2009.12.121

Huber, E., David, G., Thompson, A. J., Weiskopf, N., Mohammadi, S., & Freund, P. (2018). Dorsal and ventral horn atrophy is associated with clinical outcome after spinal cord injury. *Neurology*, *90*(17), E1510–E1522. https://doi.org/10.1212/WNL.0000000000005361

Jelescu, I. O., Palombo, M., Bagnato, F., & Schilling, K. G. (2020). Challenges for biophysical modeling of microstructure. *Journal of Neuroscience Methods*, *344*, 108861. https://doi.org/10.1016/j.jneumeth.2020.108861

Jensen, J. H., Helpern, J. A., Ramani, A., Lu, H., & Kaczynski, K. (2005). Diffusional kurtosis imaging: The quantification of non-Gaussian water diffusion by means of magnetic resonance imaging. *Magnetic Resonance in Medicine*, *53*(6), 1432–1440. https://doi.org/10.1002/mrm.20508

Jespersen, S. N., Olesen, J. L., Hansen, B., & Shemesh, N. (2018). Diffusion time dependence of microstructural parameters in fixed spinal cord. *NeuroImage*, *182*, 329–342. https://doi.org/10.1016/j.neuroimage.2017.08.039

Jezzard, P., Barnett, A. S., & Pierpaoli, C. (1998). Characterization of and correction for eddy current artifacts in echo planar diffusion imaging. *Magnetic Resonance in Medicine*, *39*(5), 801–812. https://doi.org/10.1002/mrm.1910390518

Jones, D. K., & Basser, P. J. (2004). "Squashing peanuts and smashing pumpkins": How noise distorts diffusion-weighted MR data. *Magnetic Resonance in Medicine*, *52*(5), 979–993. https://doi.org/10.1002/mrm.20283

Kharbanda, H. S., Alsop, D. C., Anderson, A. W., Filardo, G., & Hackney, D. B. (2006). Effects of cord motion on diffusion imaging of the spinal cord. *Magnetic Resonance in Medicine*, *56*(2), 334–339. https://doi.org/10.1002/mrm.20959

Koay, C. G., Chang, L. C., Carew, J. D., Pierpaoli, C., & Basser, P. J. (2006). A unifying theoretical and algorithmic framework for least squares methods of estimation in diffusion tensor imaging. *Journal of Magnetic Resonance*, *182*(1), 115–125. https://doi.org/10.1016/j.jmr.2006.06.020

Kugler, A. V., & Deppe, M. (2018). Non-lesional cerebellar damage in patients with clinically isolated syndrome: DTI measures predict early conversion into clinically definite multiple sclerosis. *NeuroImage: Clinical*, *19*, 633–639. https://doi.org/10.1016/j.nicl.2018.04.028

Le Bihan, D., Breton, E., Lallemand, D., Aubin, M. L., Vignaud, J., & Laval-Jeantet, M. (1988). Separation of diffusion and perfusion in intravoxel incoherent motion MR imaging. *Radiology*, *168*(2), 497–505. https://doi.org/10.1148/radiology.168.2.3393671

Leemans, A., Jeurissen, B., Sijbers, J., & Jones, D. K. (2009). ExploreDTI: A Graphical Toolbox for Processing, Analyzing, and Visualizing Diffusion MR Data. *Proceedings of the 17th Scientific Meeting, International Society for Magnetic Resonance in Medicine, Honolulu, USA*, 3537. https://archive.ismrm.org/2009/3537.html

Littlejohns, T. J., Holliday, J., Gibson, L. M., Garratt, S., Oesingmann, N., Alfaro-Almagro, F., Bell, J. D., Boultwood, C., Collins, R., Conroy, M. C., Crabtree, N., Doherty, N., Frangi, A. F., Harvey, N. C., Leeson, P., Miller, K. L., Neubauer, S., Petersen, S. E., Sellors, J., … Allen, N. E. (2020). The UK Biobank imaging enhancement of 100,000 participants: rationale, data collection, management and future directions. *Nature Communications*, *11*(1), 1–12. https://doi.org/10.1038/s41467-

020-15948-9
Mangin, J. F., Poupon, C., Clark, C., Le Bihan, D., & Bloch, I. (2002). Distortion correction and robust tensor estimation for MR diffusion imaging. *Medical Image Analysis*, *6*(3), 191–198. https://doi.org/10.1016/S1361-8415(02)00079-8
Margoni, M., Petracca, M., Schiavi, S., Fabian, M., Miller, A., Lublin, F. D., & Inglese, M. (2019). Axonal water fraction as marker of white matter injury in primary-progressive multiple sclerosis: a longitudinal study. *European Journal of Neurology*, *26*(8), 1068–1074. https://doi.org/10.1111/ene.13937
Martin, A. R., Aleksanderek, I., Cohen-Adad, J., Tarmohamed, Z., Tetreault, L., Smith, N., Cadotte, D. W., Crawley, A., Ginsberg, H., Mikulis, D. J., & Fehlings, M. G. (2016). Translating state-of-the-art spinal cord MRI techniques to clinical use: A systematic review of clinical studies utilizing DTI, MT, MWF, MRS, and fMRI. *NeuroImage: Clinical*, *10*, 192–238. https://doi.org/10.1016/j.nicl.2015.11.019
Meinzer, M., Mohammadi, S., Kugel, H., Schiffbauer, H., Flöel, A., Albers, J., Kramer, K., Menke, R., Baumgärtner, A., Knecht, S., Breitenstein, C., & Deppe, M. (2010). Integrity of the hippocampus and surrounding white matter is correlated with language training success in aphasia. *NeuroImage*, *53*(1), 283–290. https://doi.org/10.1016/j.neuroimage.2010.06.004
Miller, A. J., & Joseph, P. M. (1993). The use of power images to perform quantitative analysis on low SNR MR images. *Magnetic Resonance Imaging*, *11*(7), 1051–1056. https://doi.org/10.1016/0730-725X(93)90225-3
Miller, S. P., Vigneron, D. B., Henry, R. G., Bohland, M. A., Ceppi-Cozzio, C., Hoffman, C., Newton, N., Partridge, J. C., Ferriero, D. M., & Barkovich, A. J. (2002). Serial quantitative diffusion tensor MRI of the premature brain: Development in newborns with and without injury. *Journal of Magnetic Resonance Imaging*, *16*(6), 621–632. https://doi.org/10.1002/jmri.10205
Modersitzki, J. (2009). *FAIR - Flexible Algorithms for Image Registration*. Society for Industrial and Applied Mathematics (SIAM, 3600 Market Street, Floor 6, Philadelphia, PA 19104). https://epubs.siam.org/doi/pdf/10.1137/1.9780898718843.bm
Mohammadi, S., & Callaghan, M. F. (2021). Towards in vivo g-ratio mapping using MRI: Unifying myelin and diffusion imaging. *Journal of Neuroscience Methods*, *348*, 108990. https://doi.org/10.1016/j.jneumeth.2020.108990
Mohammadi, S., Carey, D., Dick, F., Diedrichsen, J., Sereno, M. I., Reisert, M., Callaghan, M. F., & Weiskopf, N. (2015b). Whole-brain in-vivo measurements of the axonal G-ratio in a group of 37 healthy volunteers. *Frontiers in Neuroscience*, *9*, 1–13. https://doi.org/10.3389/fnins.2015.00441
Mohammadi, S., Freund, P., Feiweier, T., Curt, A., & Weiskopf, N. (2013). The impact of post-processing on spinal cord diffusion tensor imaging. *NeuroImage*, *70*, 377–385. https://doi.org/10.1016/j.neuroimage.2012.12.058
Mohammadi, S., Möller, H. E., Kugel, H., Müller, D. K., & Deppe, M. (2010). Correcting eddy current and motion effects by affine whole-brain registrations: Evaluation of three-dimensional distortions and comparison with slicewise correction. *Magnetic Resonance in Medicine*, *64*(4), 1047–1056. https://doi.org/10.1002/mrm.22501
Mohammadi, S., Tabelow, K., Ruthotto, L., Feiweier, T., Polzehl, J., & Weiskopf, N. (2015a). High-resolution diffusion kurtosis imaging at 3T enabled by advanced post-processing. *Frontiers in Neuroscience*, *9*, 427. https://doi.org/10.3389/fnins.2014.00427
Mollink, J., Kleinnijenhuis, M., van Cappellen van Walsum, A.-M., Sotiropoulos, S. N., Cottaar, M., Mirfin, C., Heinrich, M. P., Jenkinson, M., Pallebage-Gamarallage, M., Ansorge, O., Jbabdi, S., & Miller, K. L. (2017). Evaluating fibre orientation dispersion in white matter: Comparison of diffusion MRI, histology and polarized light imaging. *NeuroImage*, *157*, 561–574. https://doi.org/10.1016/j.neuroimage.2017.06.001
Novikov, D. S. (2021). The present and the future of microstructure MRI: From a paradigm shift to normal science. *Journal of Neuroscience Methods*, *351*. https://doi.org/10.1016/j.jneumeth.2020.108947
Novikov, D. S., Fieremans, E., Jespersen, S. N., & Kiselev, V. G. (2019). Quantifying brain

microstructure with diffusion MRI: Theory and parameter estimation. *NMR in Biomedicine*, *32*(4). https://doi.org/10.1002/nbm.3998

Novikov, D. S., Veraart, J., Jelescu, I. O., & Fieremans, E. (2018). Rotationally-invariant mapping of scalar and orientational metrics of neuronal microstructure with diffusion MRI. *NeuroImage*, *174*, 518–538. https://doi.org/10.1016/j.neuroimage.2018.03.006

Oeschger, J. M., Tabelow, K., & Mohammadi, S. (2023a). Axisymmetric diffusion kurtosis imaging with Rician bias correction: A simulation study. *Magnetic Resonance in Medicine*, *89*(2), 787–799. https://doi.org/10.1002/mrm.29474

Oeschger, J. M., Tabelow, K., & Mohammadi, S. (2023b). Investigating apparent differences between standard DKI and axisymmetric DKI and its consequences for biophysical parameter estimates. *BioRxiv*, 2023.06.21.545891. https://doi.org/10.1101/2023.06.21.545891

Paschoal, A. M., Zotin, M. C. Z., da Costa, L. M., dos Santos, A. C., & Leoni, R. F. (2022). Feasibility of intravoxel incoherent motion in the assessment of tumor microvasculature and blood–brain barrier integrity: a case-based evaluation of gliomas. *Magnetic Resonance Materials in Physics, Biology and Medicine*, *35*(1), 17–27. https://doi.org/10.1007/s10334-021-00987-0

Perone, C. S., Calabrese, E., & Cohen-Adad, J. (2018). Spinal cord gray matter segmentation using deep dilated convolutions. *Scientific Reports*, *8*(1), 1–13. https://doi.org/10.1038/s41598-018-24304-3

Pierpaoli, C., Walker, L., Irfanoglu, M. O., Barnett, A., Basser, P., Chang, L.-C., Koay, C., Pajevic, S., Rohde, G., Sarlls, J., & Wu, M. (2010). TORTOISE: an integrated software package for processing of diffusion MRI data. *Proceedings of the 18th Scientific Meeting, International Society for Magnetic Resonance in Medicine, Stockholm, Sweden*, abstract #1597.

Polzehl, J., & Tabelow, K. (2016). Low SNR in diffusion MRI models. *Journal of the American Statistical Association*, *111*(516), 1480–1490. https://doi.org/10.1080/01621459.2016.1222284

Raja, R., Sinha, N., Saini, J., Mahadevan, A., Rao, K. N., & Swaminathan, A. (2016). Assessment of tissue heterogeneity using diffusion tensor and diffusion kurtosis imaging for grading gliomas. *Neuroradiology*, *58*(12), 1217–1231. https://doi.org/10.1007/s00234-016-1758-y

Roebroeck, A., Miller, K. L., & Aggarwal, M. (2019). Ex vivo diffusion MRI of the human brain: Technical challenges and recent advances. *NMR in Biomedicine*, *32*(4), e3941. https://doi.org/10.1002/nbm.3941

Rohde, G. K., Barnett, A. S., Basser, P. J., Marenco, S., & Pierpaoli, C. (2004). Comprehensive approach for correction of motion and distortion in diffusion-weighted MRI. *Magnetic Resonance in Medicine*, *51*(1), 103–114. https://doi.org/10.1002/mrm.10677

Rousseeuw, P. J., & Croux, C. (1993). Alternatives to the median absolute deviation. *Journal of the American Statistical Association*, *88*(424), 1273–1283. https://doi.org/10.1080/01621459.1993.10476408

Ruthotto, L., Kugel, H., Olesch, J., Fischer, B., Modersitzki, J., Burger, M., & Wolters, C. H. (2012). Diffeomorphic susceptibility artifact correction of diffusion-weighted magnetic resonance images. *Physics in Medicine and Biology*, *57*(18), 5715–5731. https://doi.org/10.1088/0031-9155/57/18/5715

Ruthotto, L., Mohammadi, S., Heck, C., Modersitzki, J., & Weiskopf, N. (2013). Hyperelastic susceptibility artifact correction of DTI in SPM. *Proceedings of the German Workshop on Medical Image Computing (Informatik Aktuell), Heidelberg, Germany*, 344–349. https://doi.org/10.1007/978-3-642-36480-8_60

Salvador, R., Peña, A., Menon, D. K., Carpenter, T. A., Pickard, J. D., & Bullmore, E. T. (2005). Formal characterization and extension of the linearized diffusion tensor model. *Human Brain Mapping*, *24*(2), 144–155. https://doi.org/10.1002/hbm.20076

Scholz, J., Klein, M. C., Behrens, T. E. J., & Johansen-Berg, H. (2009). Training induces changes in white-matter architecture. *Nature Neuroscience*, *12*(11), 1370–1371. https://doi.org/10.1038/nn.2412

Sébille, S. B., Rolland, A. S., Welter, M. L., Bardinet, E., & Santin, M. D. (2019). Post mortem high resolution diffusion MRI for large specimen imaging at 11.7 T with 3D segmented echo-planar imaging. *Journal of Neuroscience Methods*, *311*, 222–234.

https://doi.org/10.1016/j.jneumeth.2018.10.010
Seif, M., David, G., Huber, E., Vallotton, K., Curt, A., & Freund, P. (2020). Cervical cord neurodegeneration in traumatic and non-traumatic spinal cord injury. *Journal of Neurotrauma*, *37*(6), 860–867. https://doi.org/10.1089/neu.2019.6694
Sijbers, J., den Dekker, A. J., Scheunders, P., & Van Dyck, D. (1998). Maximum-likelihood estimation of rician distribution parameters. *IEEE Transactions on Medical Imaging*, *17*(3), 357–361. https://doi.org/10.1109/42.712125
Smith, S. M., Jenkinson, M., Woolrich, M. W., Beckmann, C. F., Behrens, T. E. J., Johansen-Berg, H., Bannister, P. R., De Luca, M., Drobnjak, I., Flitney, D. E., Niazy, R. K., Saunders, J., Vickers, J., Zhang, Y., De Stefano, N., Brady, J. M., & Matthews, P. M. (2004). Advances in functional and structural MR image analysis and implementation as FSL. *NeuroImage*, *23*(Suppl. 1), S208–S219. https://doi.org/10.1016/j.neuroimage.2004.07.051
Snoussi, H., Cohen-Adad, J., Commowick, O., Combes, B., Bannier, E., Leguy, S., Kerbrat, A., Barillot, C., & Caruyer, E. (2021). Evaluation of distortion correction methods in diffusion MRI of the spinal cord. *ArXiv*. https://arxiv.org/abs/2108.03817v1
Sotiropoulos, S. N., Moeller, S., Jbabdi, S., Xu, J., Andersson, J. L., Auerbach, E. J., Yacoub, E., Feinberg, D., Setsompop, K., Wald, L. L., Behrens, T. E. J., Ugurbil, K., & Lenglet, C. (2013). Effects of image reconstruction on fiber orientation mapping from multichannel diffusion MRI: Reducing the noise floor using SENSE. *Magnetic Resonance in Medicine*, *70*(6), 1682–1689. https://doi.org/10.1002/mrm.24623
Stejskal, E. O., & Tanner, J. E. (1965). Spin diffusion measurements: Spin echoes in the presence of a time-dependent field gradient. *The Journal of Chemical Physics*, *42*(1), 288–292. https://doi.org/10.1063/1.1695690
Stroman, P. W., Wheeler-Kingshott, C., Bacon, M., Schwab, J. M., Bosma, R., Brooks, J., Cadotte, D., Carlstedt, T., Ciccarelli, O., Cohen-Adad, J., Curt, A., Evangelou, N., Fehlings, M. G., Filippi, M., Kelley, B. J., Kollias, S., Mackay, A., Porro, C. A., Smith, S., … Tracey, I. (2014). The current state-of-the-art of spinal cord imaging: Methods. *NeuroImage*, *84*, 1070–1081. https://doi.org/10.1016/j.neuroimage.2013.04.124
Sullivan, E. V., Rohlfing, T., & Pfefferbaum, A. (2010). Quantitative fiber tracking of lateral and interhemispheric white matter systems in normal aging: Relations to timed performance. *Neurobiology of Aging*, *31*(3), 464–481. https://doi.org/10.1016/j.neurobiolaging.2008.04.007
Summers, P., Staempfli, P., Jaermann, T., Kwiecinski, S., & Kollias, S. S. (2006). A preliminary study of the effects of trigger timing on diffusion tensor imaging of the human spinal cord. *American Journal of Neuroradiology*, *27*(9), 1952–1961.
Szturm, T., Kolesar, T. A., Mahana, B., Goertzen, A. L., Hobson, D. E., Marotta, J. J., Strafella, A. P., & Ko, J. H. (2021). Changes in metabolic activity and gait function by dual-task cognitive game-based treadmill system in Parkinson's disease: Protocol of a randomized controlled trial. *Frontiers in Aging Neuroscience*, *13*, 283. https://doi.org/10.3389/fnagi.2021.680270
Tabelow, K., Balteau, E., Ashburner, J., Callaghan, M. F., Draganski, B., Helms, G., Kherif, F., Leutritz, T., Lutti, A., Phillips, C., Reimer, E., Ruthotto, L., Seif, M., Weiskopf, N., Ziegler, G., & Mohammadi, S. (2019). hMRI – A toolbox for quantitative MRI in neuroscience and clinical research. *NeuroImage*, *194*, 191–210. https://doi.org/10.1016/j.neuroimage.2019.01.029
Tabelow, K., Mohammadi, S., Weiskopf, N., & Polzehl, J. (2015). POAS4SPM: a toolbox for SPM to denoise diffusion MRI data. *Neuroinformatics*, *13*(1), 19–29. https://doi.org/10.1007/s12021-014-9228-3
Tabesh, A., Jensen, J. H., Ardekani, B. A., & Helpern, J. A. (2011). Estimation of tensors and tensor-derived measures in diffusional kurtosis imaging. *Magnetic Resonance in Medicine*, *65*(3), 823–836. https://doi.org/10.1002/mrm.22655
Taylor, P. A., & Saad, Z. S. (2013). FATCAT: (An Efficient) functional and tractographic connectivity analysis toolbox. *Brain Connectivity*, *3*(5), 523–535. https://doi.org/10.1089/brain.2013.0154
Tournier, J. D., Smith, R., Raffelt, D., Tabbara, R., Dhollander, T., Pietsch, M., Christiaens, D., Jeurissen, B., Yeh, C. H., & Connelly, A. (2019). MRtrix3: A fast, flexible and open software framework for medical image processing and visualisation. *NeuroImage*, *202*, 116137.

https://doi.org/10.1016/j.neuroimage.2019.116137
Urbach, H., Flacke, S., Keller, E., Textor, J., Berlis, A., Hartmann, A., Reul, J., Solymosi, L., & Schild, H. H. (2000). Detectability and detection rate of acute cerebral hemisphere infarcts on CT and diffusion-weighted MRI. *Neuroradiology*, *42*(10), 722–727. https://doi.org/10.1007/s002340000401
Vallotton, K., David, G., Hupp, M., Pfender, N., Cohen-Adad, J., Fehlings, M. G., Samson, R. S., Gandini Wheeler-Kingshott, C. A. M., Curt, A., Freund, P., & Seif, M. (2021). Tracking white and gray matter degeneration along the spinal cord axis in degenerative cervical myelopathy. *Journal of Neurotrauma*, *38*(21), 2978–2987. https://doi.org/10.1089/neu.2021.0148
Van Essen, D. C., Smith, S. M., Barch, D. M., Behrens, T. E. J., Yacoub, E., & Ugurbil, K. (2013). The WU-Minn Human Connectome Project: An overview. *NeuroImage*, *80*, 62–79. https://doi.org/10.1016/j.neuroimage.2013.05.041
Van Essen, D. C., Ugurbil, K., Auerbach, E., Barch, D., Behrens, T. E. J., Bucholz, R., Chang, A., Chen, L., Corbetta, M., Curtiss, S. W., Della Penna, S., Feinberg, D., Glasser, M. F., Harel, N., Heath, A. C., Larson-Prior, L., Marcus, D., Michalareas, G., Moeller, S., … Yacoub, E. (2012). The Human Connectome Project: A data acquisition perspective. *NeuroImage*, *62*, 2222–2231. https://doi.org/10.1016/j.neuroimage.2012.02.018
Veraart, J., Novikov, D. S., Christiaens, D., Ades-aron, B., Sijbers, J., & Fieremans, E. (2016). Denoising of diffusion MRI using random matrix theory. *NeuroImage*, *142*, 394–406. https://doi.org/10.1016/j.neuroimage.2016.08.016
Veraart, J., Rajan, J., Peeters, R. R., Leemans, A., Sunaert, S., & Sijbers, J. (2013a). Comprehensive framework for accurate diffusion MRI parameter estimation. *Magnetic Resonance in Medicine*, *70*(4), 972–984. https://doi.org/10.1002/mrm.24529
Veraart, J., Sijbers, J., Sunaert, S., Leemans, A., & Jeurissen, B. (2013b). Weighted linear least squares estimation of diffusion MRI parameters: Strengths, limitations, and pitfalls. *NeuroImage*, *81*, 335–346. https://doi.org/10.1016/j.neuroimage.2013.05.028
Veraart, J., Van Hecke, W., & Sijbers, J. (2011). Constrained maximum likelihood estimation of the diffusion kurtosis tensor using a Rician noise model. *Magnetic Resonance in Medicine*, *66*(3), 678–686. https://doi.org/10.1002/mrm.22835
Weiskopf, N., Edwards, L. J., Helms, G., Mohammadi, S., & Kirilina, E. (2021). Quantitative magnetic resonance imaging of brain anatomy and in vivo histology. *Nature Reviews Physics*, *3*, 570–588. https://doi.org/10.1038/s42254-021-00326-1
Yiannakas, M. C., Kearney, H., Samson, R. S., Chard, D. T., Ciccarelli, O., Miller, D. H., & Wheeler-Kingshott, C. A. M. (2012). Feasibility of grey matter and white matter segmentation of the upper cervical cord in vivo: A pilot study with application to magnetisation transfer measurements. *NeuroImage*, *63*(3), 1054–1059. https://doi.org/10.1016/j.neuroimage.2012.07.048
Zhang, H., Schneider, T., Wheeler-Kingshott, C. A., & Alexander, D. C. (2012). NODDI: Practical in vivo neurite orientation dispersion and density imaging of the human brain. *NeuroImage*, *61*(4), 1000–1016. https://doi.org/10.1016/j.neuroimage.2012.03.072
Zwiers, M. P. (2010). Patching cardiac and head motion artefacts in diffusion-weighted images. *NeuroImage*, *53*(2), 565–575. https://doi.org/10.1016/j.neuroimage.2010.06.014